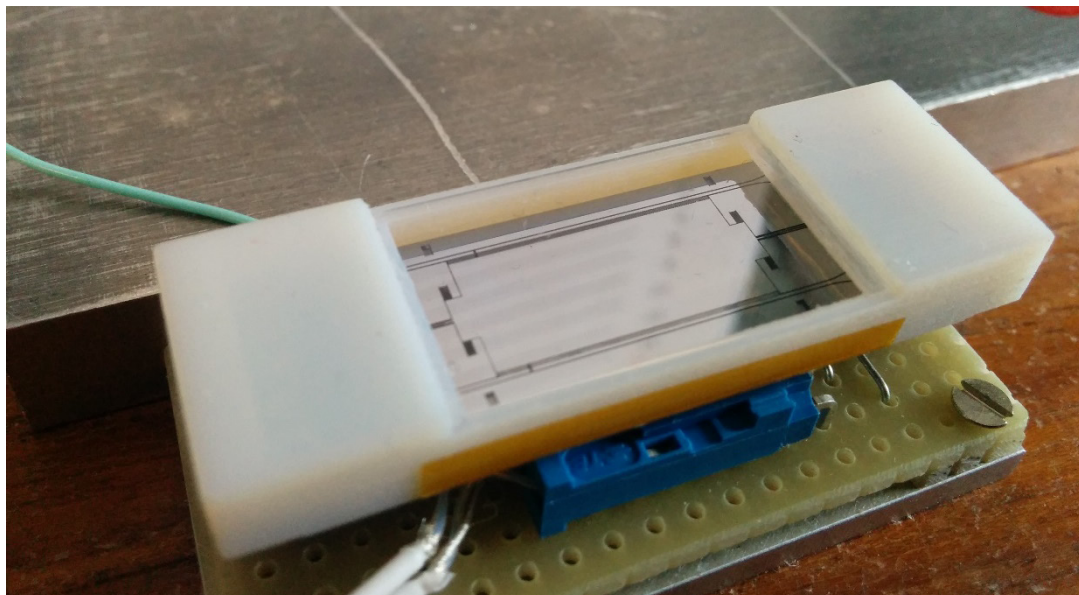


Imperial College London

Department of Electrical and Electronic Engineering

Final Year Project Report 2015



Project Title: **Control of a MEMS Scanning Mirror for Display Applications**

Student: **Kishan Amratia**

CID: **00694139**

Course: **EE4T**

Project Supervisor: **Professor Andrew Holmes**

Second Marker: **Professor Richard Syme**

Abstract

Micro-Electro-Mechanical Systems (MEMS) has facilitated the miniaturisation of image projection technologies, in particular the MEMS scanning mirror. This report discusses the simulation, design and manufacture of an optimized driver for a large area silicon MEMS scanning mirror for head-up-display applications. The device is based on a torsional mirror excited by electrostatic actuators that exhibit highly non-linear behaviour. To study this non-linear behaviour and the device dynamics, the mirror has been modelled in MATLAB Simulink together with force calculations on the actuators based on a conformal mapping technique known as the Schwarz-Christoffel Transformation. The driver circuit designed is a closed loop controller that monitors mirror position via capacitance sensing and generates suitable excitation signals. A prototype scanning mirror has been tested with the driver and the performance evaluated against the simulation results. In this project, the closed loop controller has been demonstrated to drive the mirror, however, future work can investigate other capacitance measurement circuits and additional control algorithms to reduce jitter.

Acknowledgements

First of all, I would like to thank Professor Andrew Holmes for his continuous support and supervision throughout this project. I would also like to thank Mr Vic Boddy for helping with soldering of QFN32 package integrated circuits and also his support and advice while working in the lab. I am also grateful to Professor Toby Driscoll for providing the MATLAB SC Transformation Toolbox as open source that made accurate simulations possible.

Finally, I would like to thank my family and friends for their continuous support but most importantly I would like to thank my parents for their support and blessing throughout the course of my degree.

Contents

Abstract	1
Acknowledgements	2
1 Introduction.....	5
2 Background.....	7
2.1 History of MEMS	7
2.2 MEMS Scanning Mirrors.....	8
2.2.1 Operating Principle	8
2.2.2 Commercial Development.....	10
2.2.3 OSD Group, Imperial College London	10
2.3 Out-of-Plane Comb Drive Analysis and Mirror Driving Principle.....	11
2.4 Mirror Structure and Dimensions	13
3 Project Requirements	16
4 Simulation	17
4.1 Mathematical Modelling	17
4.2 Determining Torque	18
4.2.1 Schwarz-Christoffel mapping	18
4.2.2 SC Transformation MATLAB Toolbox	20
4.2.3 Torque Calculation	21
4.3 MATLAB Simulink Modelling	24
4.3.1 Simulink Model Creation.....	24
4.3.2 Open Loop Simulation	25
4.3.3 Closed Loop Simulation.....	26
5 Design.....	30
5.1 High Level Design	30
5.2 High Voltage Converter Design.....	31
5.3 Capacitance Sensing Method	34
5.4 Microcontroller	35
5.5 Differences from Initial Design	36
6 Implementation	38
6.1 HV Converter	38
6.2 Capacitance Sensor	40
6.3 Software.....	41
6.3.1 ADC Setup	41
6.3.2 Control Algorithm	42
6.3.3 RTX RTOS.....	43
6.3.4 PC Interfacing and Serial Debugging.....	44

6.4	Final Printed Circuit Board.....	45
6.4.1	Input Protection and Power Circuitry	45
6.4.2	PCB Design and Size	46
7	Testing and Results.....	48
7.1	Test Setup	48
7.2	Open Loop Tests	49
7.2.1	Mirror Properties and Transient Coupling.....	49
7.2.2	Resonant Frequency	50
7.2.3	Test Results.....	51
7.2.4	Phase Delay and Capacitance Measurement.....	52
7.3	Closed Loop Tests	53
7.3.1	Control Algorithm Testing and Phase Delay Compensation	53
7.3.2	Test Results.....	53
7.4	Comparison with Simulation Results.....	54
8	Project Evaluation.....	57
8.1	Simulation Model Evaluation.....	57
8.2	Hardware Evaluation.....	57
9	Future Work	59
9.1	Other Capacitance Measurement Circuits	59
9.2	SPI Interfacing	59
9.3	Improved Control Algorithms to Reduce Jitter	59
10	Conclusion	60
	Bibliography.....	61
	Appendix	64
A.	MATLAB Simulation Setup.....	64
B.	Circuit Schematics	66
C.	Notes on Circuit schematic and PCB design files	68
D.	Bill of Materials (BoM).....	69
E.	Microcontroller Software Setup and Programming	71
F.	PICOCAP Device Programming and using the GUI	74

1 Introduction

Micro Electro-Mechanical Systems (MEMS) are tiny integrated devices ranging in size from a few microns to a few millimetres. They combine mechanical and electrical components using silicon fabrication techniques employed in integrated circuit fabrication. The interdisciplinary nature of MEMS has allowed the miniaturization of multiple sensors, transducers and actuators. One such example is the accelerometer, which is used in today's smart phones to detect position but more importantly was first used to detect the deceleration of a vehicle in the event of a crash and thus deploying the air-bags. Such devices can be built in large quantities at low cost and can be proven to be more reliable than previous technology making them cost-effective. Additionally, MEMS devices, specifically MEMS scanning mirrors are also used in optical applications such as projection displays. Details of how MEMS scanning mirrors are used in projection displays is described in the section 2.2.1 of this report.

The Optical Semiconductor Devices (OSD) group in the Electrical and Electronic Engineering (EEE) Department at Imperial College London are developing a large area single axis silicon MEMS scanning mirror for head-up-display applications. It is based on a torsional mirror excited by electrostatic actuators that exhibit highly non-linear behaviour. This project involves the analysis and simulation of the device dynamics followed by the design and manufacture of an optimized driver. This is a closed loop controller that monitors mirror position by capacitance sensing and generates appropriate excitation signals. Figure 1.1 shows an image of the MEMS scanning mirror.

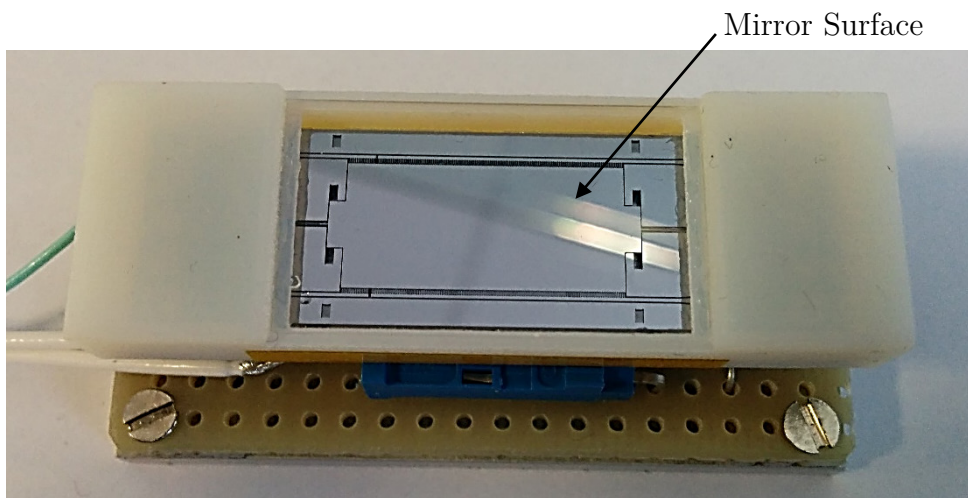


Figure 1.1: Image of a prototype MEMS scanning mirror developed by the OSD Group. It is mounted on a carrier to allow easy access to the actuators.

To study the device dynamics, a MATLAB Simulink model has been created to observe the behaviour of the mirror under different parameters in open loop operation and also optimize a driver for closed loop operation. The information gained from the simulation helped in the design of an electronic driver, especially in knowing the type and magnitude of excitation signals needed and the capacitance measurement range required in order to detect mirror position. The electronics design has the following components:

- Design of an adjustable Low-High Voltage DC-DC converter to generate the excitation signals
- A capacitance measurement circuit
- Selection of a suitable microcontroller and development of software to carry out the control algorithm that generates the excitation signals through information about the mirror position inferred from the capacitance measurement.

The hardware and microcontroller software have been developed and tested individually. Due to fabrication delays, the prototype mirror was not available for testing until the beginning of June 2015. Therefore, improvements to the controller were not possible before the end of the project. However, regardless of the limited time, closed loop control was achieved but couldn't be optimised.

This report briefly introduces some background on MEMS scanning mirrors and thereafter concentrates on the design and simulation of a suitable mirror model. This is followed by a detailed description of the design, implementation and testing of the electronic controller. The report ends with a critical evaluation along with a section on future work and a conclusion. Support material for further development is provided in the Appendix.

2 Background

2.1 History of MEMS

Following the invention of the first semiconductor transistor, the fabrication technologies behind integrated circuits rapidly developed from the 1960s to the 1980s [1]. The micromachining of silicon using single-crystal or polycrystalline silicon was already used in IC technology and was simply adopted to create three dimension mechanical structures [2]. This technology together with the use of anisotropic¹ silicon etching to create three-dimensional features in planar silicon substrates [3] paved the way to creating micromechanical devices such as cantilevers, membranes and nozzles. This eventually led to the invention of the silicon micro-machined nozzle ink-jet printer by Hewlett-Packard in 1978. This offered a low-cost alternative to laser printing and could also print high quality colour images [4]. The use of micromachining to describe this field was quite common but ultimately, the term MEMS was introduced and became widely accepted as the field expanded rapidly into the 1990s.

Other than the inkjet nozzles, early MEMS devices that gained recognition are the integrated inertia sensors (accelerometers) for use in car air-bag deployment and also the digital light processing (DLP) chip developed by Texas Instruments for projection display.

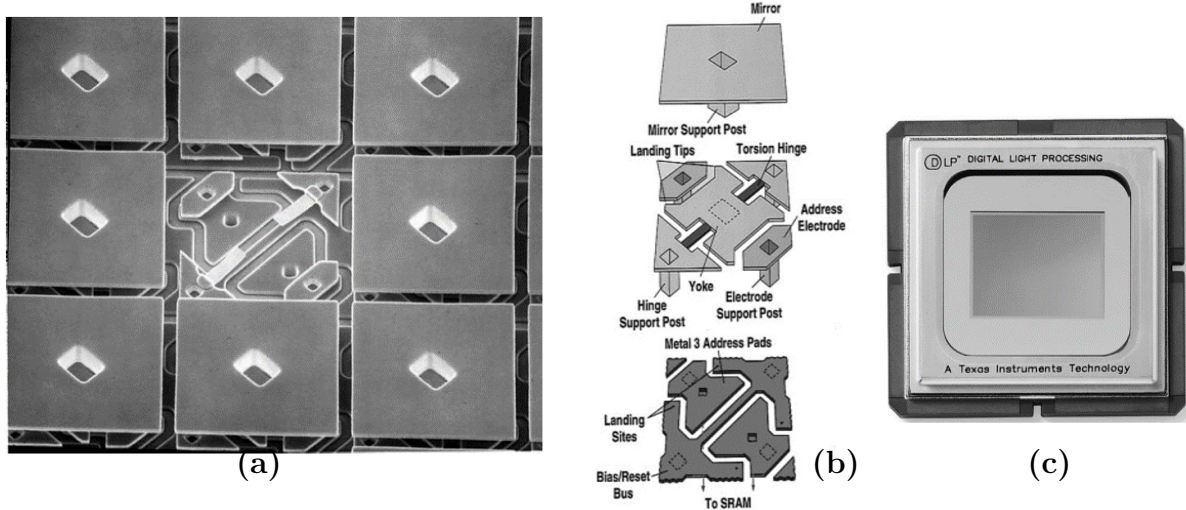


Figure 2.1: The DLP chip developed by Texas Instruments (Image Source: [5]). (a): An array of tilting micro mirrors with the centre mirror removed. (b): Schematic of the mirror actuation mechanism and mechanical support structure. (c): Complete packaged device

¹ The property of being directionally dependent, as opposed to isotropy, which implies identical properties in all directions.

The invention of the MEMS accelerometer had significant advantages over using large electro-mechanical sensors including increased sensitivity, low noise and reduced cost. Nowadays, similar technology is used in smart phones to detect position. On the other hand, the DLP was a revolutionary digital optical projection display that contained more than 100,000 individually addressable micro-mirrors to modulate light. Each mirror is capable of tilting by a small angle which when placed at the correct angle can reflect light towards a screen and illuminate a single pixel. The array of mirrors can therefore form an image on a screen.

The actuation and sensing of these MEMS devices was also an important step towards making them usable. Today, there are multiple methods of sensing the physical properties of the devices ranging from capacitive sensing, piezo-resistivity, optical interferometry among others [4]. The actuation methods of MEMS involve different principles from electrostatic, thermal, piezo-electric, and magnetic [5].

MEMS technology has played a massive role in miniaturising today's technology that many take for granted. More recent developments have integrated MEMS within biotechnology creating drug delivery systems and other applications in microfluidics as well [6,7]. It is expected that the field continues to expand with the invention of many new applications and also with the advent of nano-electromechanical systems, commonly referred to as NEMS [8].

2.2 MEMS Scanning Mirrors

2.2.1 Operating Principle

A MEMS scanning mirror is a device commonly used for imaging or display applications and has been the key driver for miniaturised projection displays. Figure 2.2 shows a diagram explaining the basic principle of a MEMS scanning mirror for display applications. Each pixel of the image is modulated by the RGB Laser diode and directed towards the scanning mirror to be reflected onto a screen. If the mirror motion is synchronous to the modulation of the laser, an image can be scanned onto a screen as shown in Figure 2.2 and hence the name "Scanning Mirror". In reality, some optics may be involved to achieve image magnification. Additionally, scanning mirrors are driven at their resonant frequencies to obtain high mechanical gain in order to achieve large oscillation amplitudes. This is the basic principle of operation of a MEMS scanning mirror for display purposes; however, the exact method of projection depends on the mirror type and device architecture.

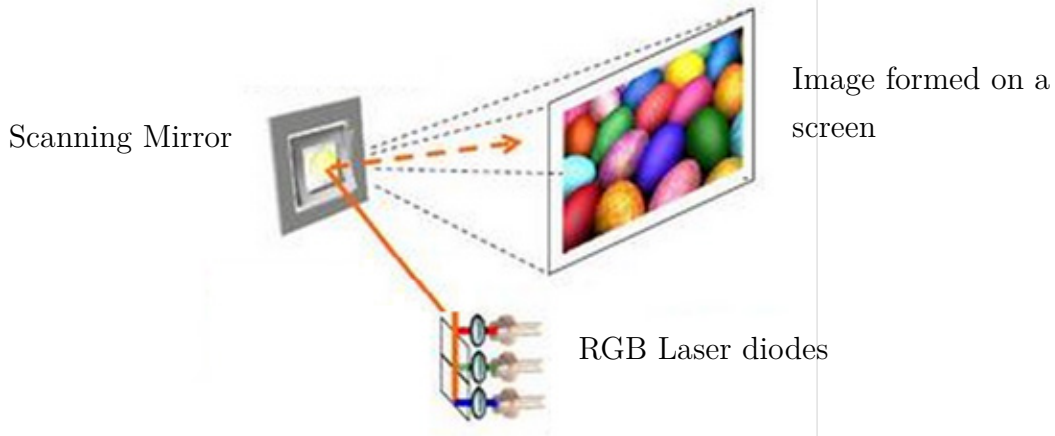


Figure 2.2: operating principle of a MEMS scanning mirror showing how an image is formed on a screen through modulation of laser diodes directed towards the scanning mirror. (Image adapted from: <http://www.electroline.com.au/articles/62086-MEMS-scanning-mirror-for-smartphone-applications>)

There are many variants of mirrors that have been developed with different types of actuators and varying properties. The review paper by Holmström, Bakan and Urey [9], reviews both one-dimensional (1D) and two-dimensional (2D) high frequency scanning mirrors developed over the last decade. These mirrors utilise a single RGB laser diode and use high scan frequencies for the mirror. An example system architecture known as flying spot laser projection is shown in Figure 4.

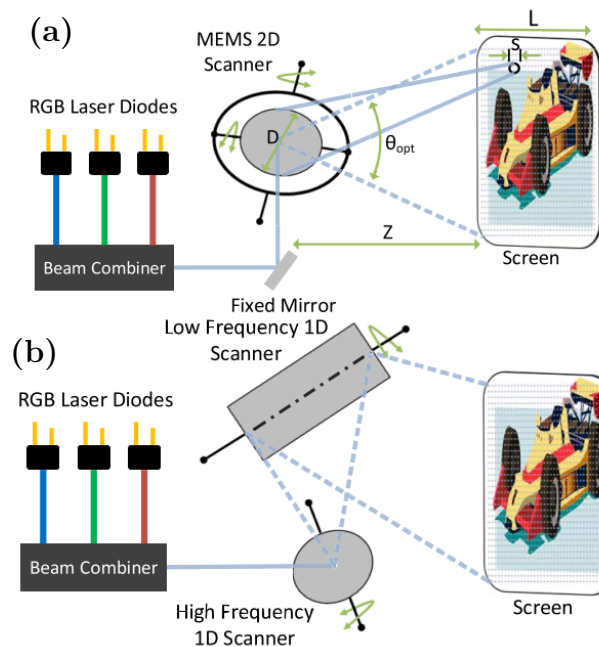


Figure 2.3: Schematic of a flying spot laser projector. (a): two-dimension scanning architecture. (b): Two one-dimensional mirrors scanning architecture. (Image source: [9])

2.2.2 Commercial Development

Commercially, there are a few companies that offer high frequency 1D and 2D scanning mirrors on the market. Table 2.1 summarises the companies and gives short descriptions of the mirrors offered by them.

Table 2.1: Scanning mirrors offered by different companies. Information in the table is gathered from the relevant company websites.

Company/ Institution	Description	Resonant Frequency (kHz)	Maximum Dimension (mm)
Franoufer IPMS	1D or 2D mirrors electromagnetically actuated.	0.1 - 50	3
Lempotix (acquired by Intel)	Magnetically actuated	-	2.5
Opus Microsystems	1D and 2D electrostatic actuated mirrors	1D: 0.5 – 2 2D: 18 – 24.5	1D: 4 2D: 8
Mirrorcle Technologies	2D electrostatic actuated mirror	1.3 - 4	4.2
Maradin Ltd.	2D mirror electromagnetically actuated	1.3	1.1

The table shows that all of the commercially developed scanning mirrors are based on small dimensions and most of them have high resonant frequencies.

2.2.3 OSD Group, Imperial College London

The OSD Group in the EEE Department at Imperial College London have developed a large area silicon MEMS scanning mirror (Figure 1.1). The dimensions of this device has two variants: 17mm x 6mm and 17mm x 8mm. These are relatively large mirrors in comparison to the commercial development summarised in Table 2.1.

The purpose of the mirror is to be used on a head-up-display application for a commercial project. The motivation for using a large mirror is based on a specific application, which uses an array of modulating LEDs encompassing the length (17mm) of the mirror. Consequently, to produce an image the mirror needs to be scanned only in one-dimension at relatively low frequencies (around 100Hz) that correspond to the refresh rate of the image.

The actuators in the mirror are based on an out-of plane electrostatic comb drive. This is an array of interdigitated electrodes as shown in Figure 2.4. When a potential difference is

present between the fixed and moving electrodes of the actuator, a torque is produced on the mirror due to the electrostatic forces pulling the moving electrodes towards the fixed electrodes.

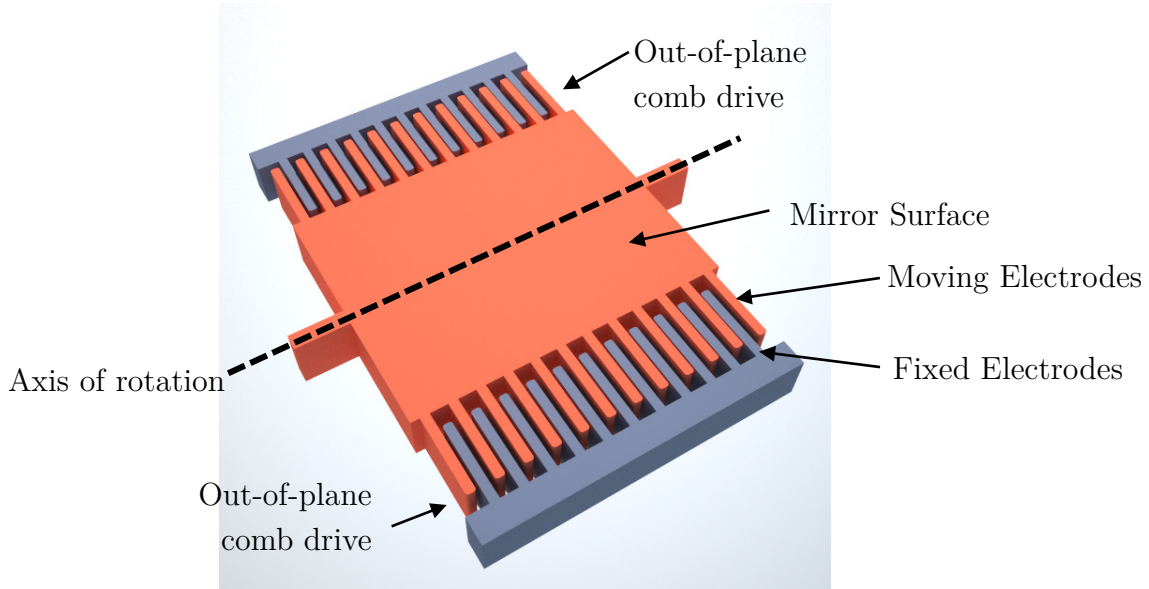


Figure 2.4: Three-Dimensional (3D) representation of the mirror showing the axis of rotation and the electrodes structure in the out-of-plane comb drive.

2.3 Out-of-Plane Comb Drive Analysis and Mirror Driving Principle

The out-of-plane electrostatic actuators in the mirror can be modelled by a varying overlap of a parallel-plate capacitor between a moving mass and fixed land as shown in Figure 2.5. Using this model, we can derive an approximation to the force.

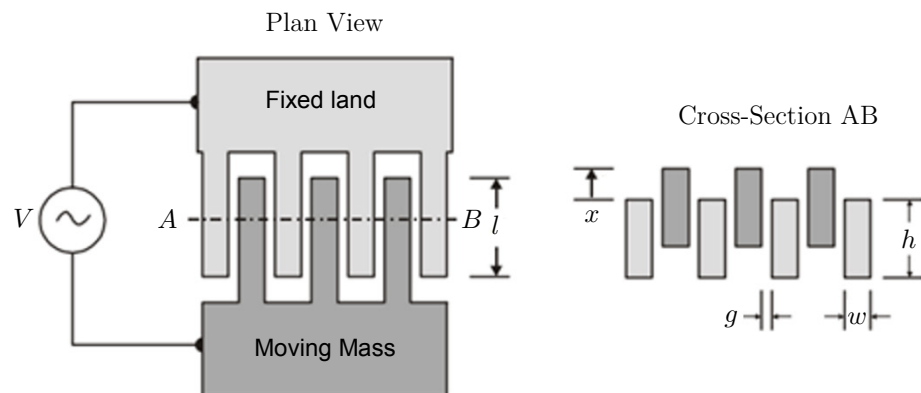


Figure 2.5: Plan and Cross-section view of an out-of-plane comb drive actuator [10]

The capacitance associated with each gap is:

$$C = \begin{cases} \frac{\varepsilon_0(h - |x|)l}{g} & |x| < h \\ 0 & otherwise \end{cases} \quad (2.1)$$

Using the principle of virtual work, the electrostatic force in the gap is given by:

$$F = \frac{\partial}{\partial x} \left(\frac{1}{2} CV^2 \right) = \frac{1}{2} V^2 \frac{\partial C}{\partial x} = \begin{cases} \frac{-N\varepsilon_0 l V^2 \operatorname{sgn}(x)}{2g} & |x| \leq h \\ 0 & otherwise \end{cases} \quad (2.2)$$

where N is the number of gaps, $\operatorname{sgn}(x)$ is the sign function and ε_0 is the permittivity of free space.

The equation of motion of the mirror is similar to that of a mass-spring-damper system and is clearly non-linear.

$$m \frac{d^2x}{dt^2} + c \frac{dx}{dt} + kx = F(x, V) \quad (2.3)$$

where:

m is the mass of the mirror, c is the damping coefficient and k is spring constant.

$\omega_0 = \sqrt{(k/m)}$ is the resonant (or un-damped natural) frequency of the system

$\zeta = c/(2m\omega_0)$ is the damping factor, which is a dimensionless parameter describing the degree of damping. This is sometimes specified in terms of quality factor: $Q = 1/2\zeta$

If the mirror has high Q (low damping), the motion of the mirror can be assumed to be approximately sinusoidal in steady-state. Additionally, if the drive voltage, V is a square wave, maximum amplitude of oscillation occurs when negative transitions in drive voltage occur at zero-crossing points and positive transitions occur at maximum and minimum points as shown in Figure 2.6.

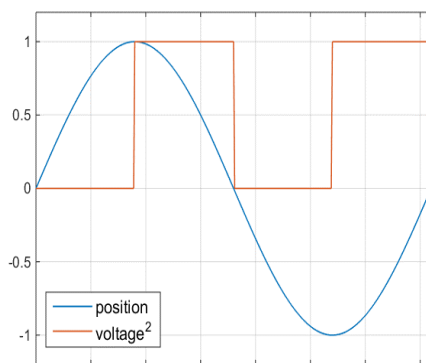


Figure 2.6: Driving principle of MEMS mirror to achieve maximum mirror oscillation amplitude using a square wave drive signal.

This suggests that using a square wave drive signal at twice the resonant frequency will result in high oscillation amplitudes. However, due to process variation in manufacturing and environmental factors, the resonant frequency of each mirror is different and not known. Therefore, driving the mirror at twice the assumed resonant frequency cannot work. In practice it is best to drive the mirror by having a voltage function dependent on both time and position. Thus a closed loop controller is required to ensure resonance. This can be done through sensing capacitance of the electrodes to detect position and applying a suitable driving voltage to the actuators.

Section 4 of this report discusses the development of an accurate model for the MEMS scanning mirror and the actuators. It considers the fringing fields that contribute towards a non-zero force for the region where $|x| > h$ unlike in equation (2.2). It also solves the non-linear differential equation of the system using MATLAB Simulink in order to estimate oscillation amplitude. A closed loop controller is also designed in the process.

2.4 Mirror Structure and Dimensions

There are two different sizes of the mirror developed by the OSD group: one has dimensions of 17mm x 6mm and the other is 17mm by 8mm. It is designed to have a resonant frequency of 100Hz. A 3D diagrammatic representation of the MEMS scanning mirror is shown in Figure 2.7 and Figure 2.8 (not to scale).

Note: The values of the dimensions marked in the figures are described in Table 2.2. These symbols and values will be used throughout the report to reference the relevant dimensions.

The main elements of the mirror annotated in Figure 2.7 are:

1. **Mirror Surface:** This surface is coated with a high reflection coefficient material such as gold to reflect light optimally.
2. **Fixed and Moving Electrodes:** These form part of the comb drive actuator system. The mirror has two electrode arrays along the lengths of the mirror.
3. **Torsion Bar:** The mirror is mounted on a torsion bar. While the mirror oscillates a torsional force is exerted on this bar which tends to bring the mirror to its rest position.

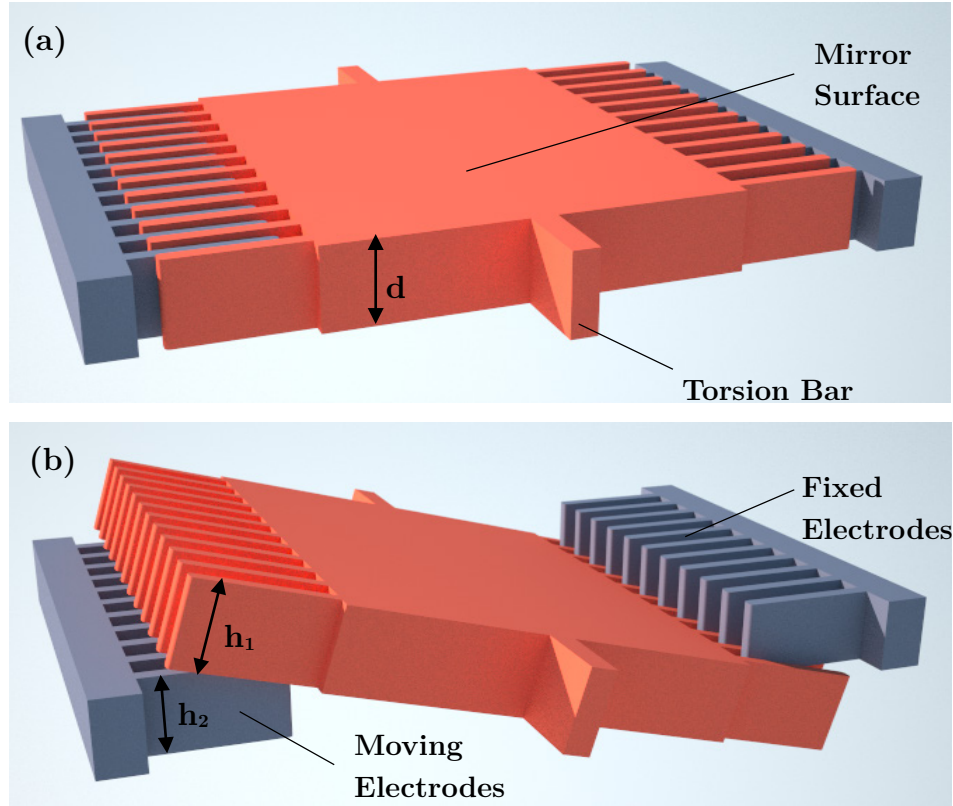


Figure 2.7: Snapshot of MEMS scanning mirror at different instances during oscillation.

(a): mirror at its nominal rest position. (b): mirror at an angle

Table 2.2: Mirror Dimensions

Dimension	Symbol	Size
Mirror length	L	17mm
Mirror width	W	6mm or 8mm
Mirror depth	d	200 μ m
Electrode overlap length	l	200 μ m
Electrode width	w	34 μ m
Inter-Electrode gap	g	16 μ m
Electrode gap at tip	p	50 μ m
Height of Moving electrodes	h_1	200 μ m
Height of Fixed electrodes	h_2	180 μ m

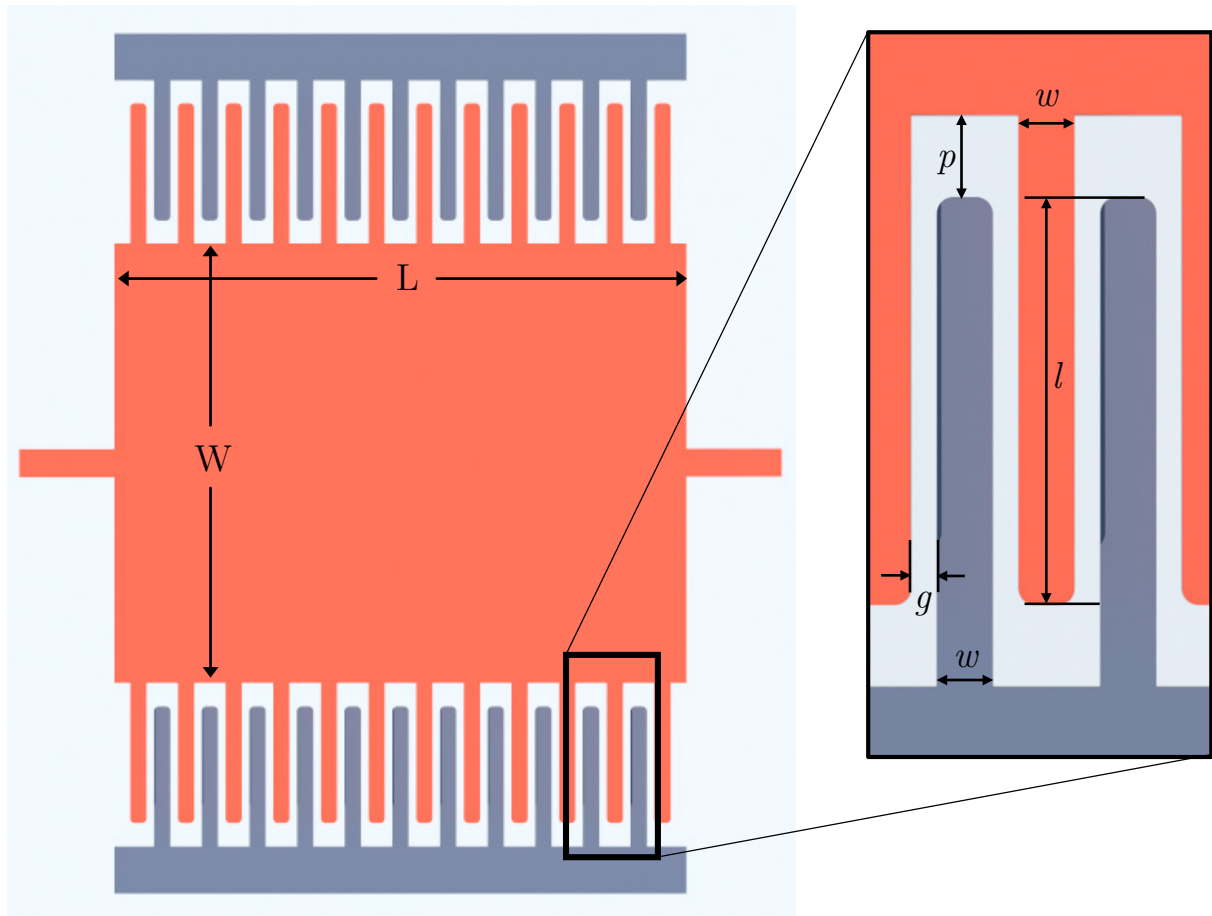


Figure 2.8: Structure of MEMS scanning mirror showing a magnification of the electrodes.

3 Project Requirements

The project is split in two phases:

1. Simulation:

This phase involves a detailed analysis of the mirror dynamics through development of a realistic simulation model. This would help in making design decisions for the second phase based on the results from the simulations.

2. Design and Manufacture:

This phase of the project requires design and implementation an optimized driver for the MEMS mirror such that it oscillates with the required amplitudes for display purposes. The following functions are required by the driver:

- Amplitude control for controlling the oscillation amplitude of the mirror.
- A synchronisation signal also needs to be generated by the driver which can be fed to an external light source to synchronise itself to the mirror such that the image projection is non-distorted.

The final driver should be able to be manufactured in the form of a PCB in a small form factor comparable the size of the MEMS device package (50mm x 25mm).

In summary, the project aim is to design and develop an optimized driver for a large area single axis MEMS scanning mirror through analysis, simulation, implementation, prototyping and finally manufacture.

4 Simulation

In order to develop a simulation model, a mathematical model must be developed first. This section discusses the development of a Simulink model based on a second order differential equation of a Forced harmonic torsional oscillator.

4.1 Mathematical Modelling

The MEMS scanning mirror can be modelled as a second order dynamic system in particular that of a Torsional Harmonic Oscillator. These types of systems oscillate with a rotational motion about the axis of the torsion bar. Their behaviour is analogous to that of a mass-spring-damper system as described by equation (2.3) in section 2.5. However, its equation of motion is defined using different terms and is given by (refer to Table 4.1 for definitions of the terms):

$$I \frac{d^2\theta}{dt^2} + C \frac{d\theta}{dt} + K\theta = T \quad (4.1)$$

Table 4.1: Definition of terms in equation (4.1)

Term	Definition	Unit
θ	Deflection angle (shown in Figure 4.1)	Radians
t	Time	Seconds
T	Driving Toque	Nm
I	Moment of inertia	Kgm ²
C	Rotational friction (damping)	Kgm ² s ⁻¹ rad ⁻¹
K	Torsion spring coefficient	Nmrad ⁻¹

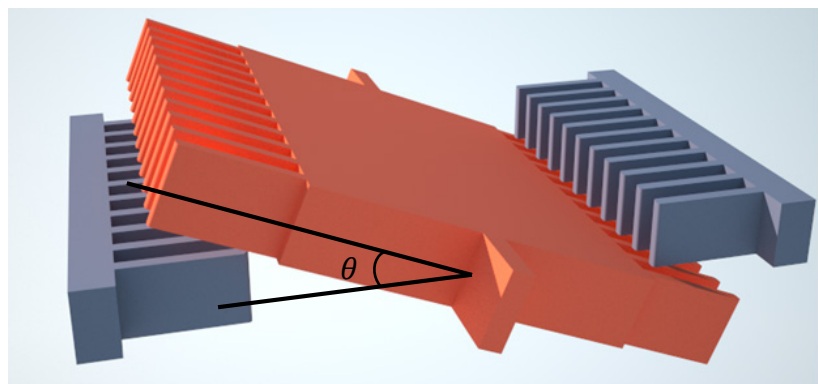


Figure 4.1: 3D representation of the mirror under oscillation. The deflection angle, θ of the mirror is shown

The system parameters, I, C and K in equation (4.1) can be calculated using the equations below:

$$I = \frac{1}{12} m W^2 \quad (4.2)$$

$$K = I \omega_n^2 \quad (4.3)$$

$$C = \frac{\sqrt{IK}}{Q} \quad (4.4)$$

Equation (4.2) calculates the moment of inertia. It assumes that the mirror is a thin rectangular plate whose mass, m , can be determined with the product of the density of silicon (2.3290 gcm⁻³) and the volume ($L \times W \times d$) of the plate. Equation (4.3) and (4.4) calculate the Torsion Spring coefficient and Rotational Friction respectively. ω_n is the resonant frequency of the system measured in rads⁻¹ and Q is the Quality factor.

The mirror has been designed to have a resonant frequency of 100Hz (628.3 rads⁻¹). If we know the quality factor, Q, we can calculate the constants I, C and K based on the mirror dimensions and the resonant frequency. The model is still incomplete without the torque function, T, which is a non-linear function of the time, t and position, θ . To obtain this function, a detailed analysis is required and is done in section 4.2.

4.2 Determining Torque

The torque on the mirror is achieved via electrostatic forces on the out-of-plane comb drive actuators. This is highly dependent on the fringing fields at the electrodes, therefore, a simple parallel-plate capacitor model of the electrodes as used in equation (2.2) cannot give accurate force calculations. Consequently, more refined methods are required such as Finite-Element-Analysis (FEA); however, this is complex and requires sophisticated software tools. In this report, the torque is determined through force calculations using a conformal mapping technique known as the Schwarz-Christoffel (SC) Mapping. This method is known to be accurate to within 5% in comparison to FEA as inferred from [11].

4.2.1 Schwarz-Christoffel mapping

The Schwarz-Christoffel mapping or SC transformation [12] is a conformal transformation to map the complex upper half-plane to the interior of a polygon or vice versa.

Figure 4.2 shows an SC transformation whereby the real-axis in the z-plane is connected to the boundary of the polygon in the w-plane and such that the points $x_1, x_2 \dots, x_n$ are mapped onto the vertices $w_1, w_2 \dots, w_n$ of the polygon with interior angles $\phi_1, \phi_2 \dots, \phi_n$ [13].

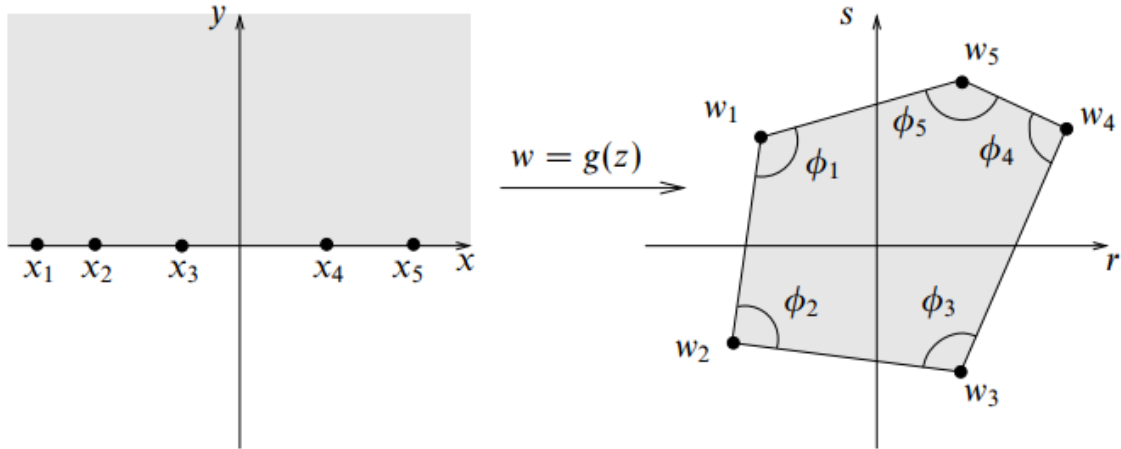


Figure 4.2: Image showing the transformation of the upper half plane in the z-plane into the interior of a polygon in the w-plane. [13]

The transformation equation [12–14] is given by:

$$w = g(z) = g(z_0) + c \int_{z_0}^z \prod_{j=1}^{n-1} (\zeta - z_j)^{\frac{\phi_j}{\pi} - 1} d\zeta \quad (4.5)$$

where c is a multiplicative constant to determine the size of the polygon and n is the number of vertices of the polygon.

The transformation given by equation (4.5) describes the mapping from the upper half plane to the polygon. Theoretically, the SC transformation allows an infinite number of points on the upper-half plane to be mapped onto the vertices on a polygon (including vertices at infinity). However, it is more desirable to have the inverse mapping, which is very difficult to do analytically and numerical techniques often need to be used.

A combination of the forward and inverse SC transforms can be used to perform a conformal mapping between the interior of an intricate polygon to the interior of a much simpler one. This is done by using the inverse mapping to map the interior of one polygon to the upper half-plane and then performing a forward transformation from the points in the upper-half plane to a simpler polygon. In the context of this project, this can be interpreted as a conformal mapping of the electric field present at the electrodes in the comb-drive actuator to a field limited to that of a true parallel plate capacitor and as a result making calculations trivial in the parallel plate capacitor domain. This is shown using MATLAB in section 4.2.2.

4.2.2 SC Transformation MATLAB Toolbox

An open source MATLAB toolbox to perform SC Transformations is very useful and can be found at <http://www.math.udel.edu/~driscoll/SC/>. It provides functions to perform inverse transformations and also other useful functions to plot the transformation mapping.

Figure 4.3 shows a plan view and a cross-section of a segment of the electrodes in the comb-drive actuator. The shaded region in the cross-section represents the area between two electrodes that can be evaluated using the SC Transformation. This obtains the electric field within the gap transformed into a rectangular domain representing a parallel-plate capacitor.

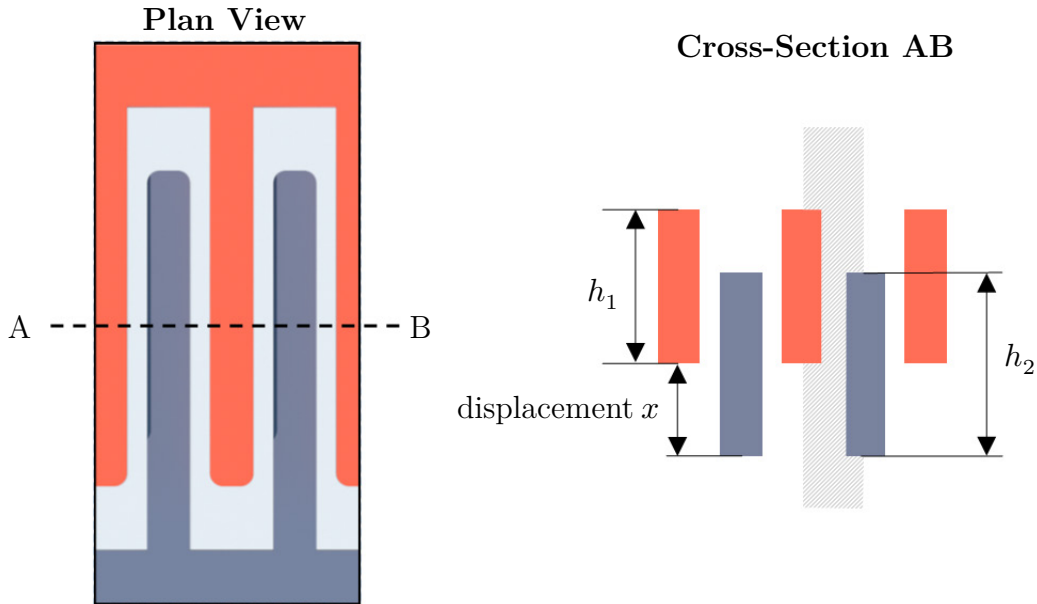


Figure 4.3: Cross-section of the electrodes in the actuator

Figure 4.4 shows a plot of the field mapping of a single gap within the electrodes and the corresponding plot in a rectangular domain. The displacement, x between the electrodes in the plot is $50\mu m$. Using the information in the rectangular domain, we can calculate the capacitance of an electrode array as:

$$C = \frac{N\epsilon_0 d_2 l}{d_1} \quad (4.6)$$

Since the gaps are symmetrical, the capacitance calculation is simply multiplied by the number of gaps, N in the electrode array. l is the overlap length of the electrodes and d_1 and d_2 are the width and length of the rectangle shown in Figure 4.4 respectively. By varying the displacement, the capacitance can be calculated as a function of the displacement. As a result, the method of virtual work can be used to determine total force and consequently the torque. This is described in section 4.2.3.

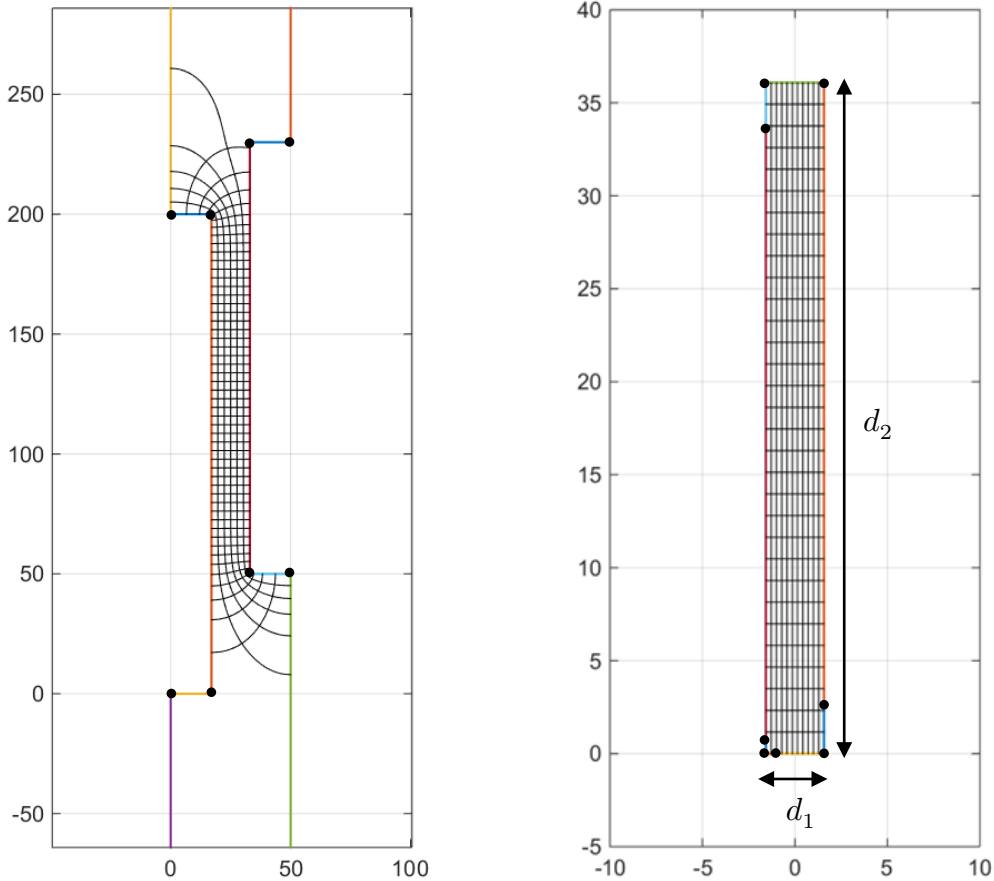


Figure 4.4: Mapping between the electrode geometry and the rectangular domain using the SC Toolbox. Dimensions in the plot are in μm

4.2.3 Torque Calculation

Torque or moment is the tendency of an object to rotate about an axis or pivot. It is calculated as the vector cross product of a force and the distance between the point of force and the axis of rotation. Figure 4.5 illustrates a side profile of the mirror with key dimensions and forces annotated.

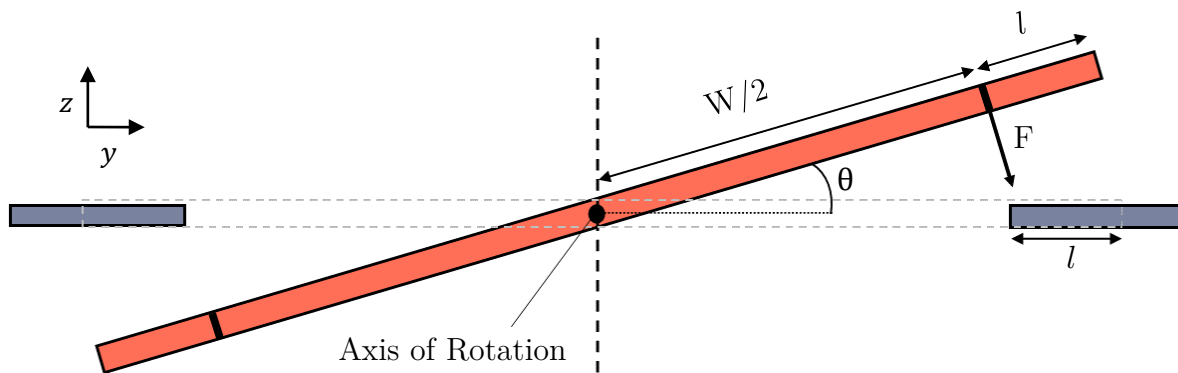


Figure 4.5: Side profile of the MEMS scanning mirror

The torque at any given mirror deflection is given by:

$$T(\theta) = F(\theta) \cdot \frac{W}{2} \quad (4.7)$$

For equation (4.7) to be valid, some assumptions are made:

1. **The force is considered to be constant along the electrode length.** Due to the deflection angle, the force along the length of the electrode varies. However, since the angle, θ , is expected to be small (< 5 degrees), the deviation of the force along the length of the electrode is also small.
2. **The force is perpendicular to the mirror surface and is acting at a single point at the edge of the mirror surface.** In reality, the force acts along the whole length of the electrode rather than at a single point and involves an integration when calculating torque to be accurate. However, the electrode length is small compared to the distance between the point of force and the axis of rotation, therefore, this assumption is valid.

Using the MATLAB SC Toolbox, the displacement in the electrodes is varied and the capacitance is calculated for each displacement and as a result, the capacitance against displacement function is obtained. By changing the variable from x to θ using trigonometry, $\theta = \sin^{-1}(2x/W)$, the capacitance against deflection angle function is obtained.

Using the principle of virtual work, the force can be calculated as $(\theta) = \frac{d}{d\theta} (\frac{1}{2} CV^2) = \frac{1}{2} V^2 \frac{dC}{d\theta}$. The torque is then calculated using equation (4.7).

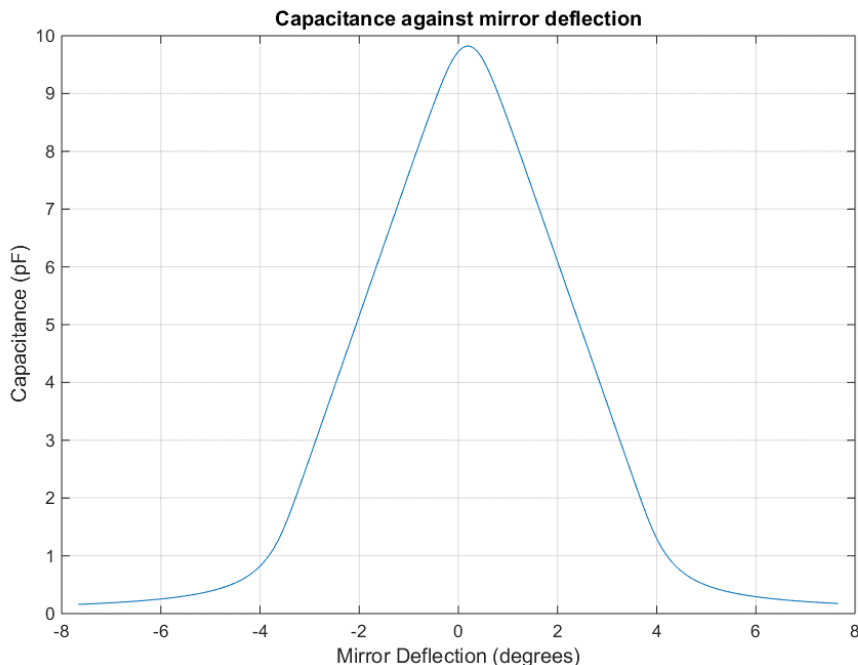


Figure 4.6: MATLAB plot of capacitance against mirror deflection

Figure 4.6 shows a plot of the capacitance against the mirror deflection calculated in MATLAB. The capacitance calculated only includes the capacitance between the electrodes for the overlap length; therefore, it only represents the change in capacitance which is enough to do perform force calculations using the method of virtual work. The actual capacitance is likely to be higher due.

Figure 4.7 shows a plot of the Normalized torque against the deflection angle for the different mirror widths ($W=6\text{mm}$ and $W = 8\text{mm}$). It is normalized such that the driving voltage is 1V. An important observation is that the plot below fits the shape of the curve dictated by equation (2.2) in section 2.3 of this report but the torque for a deflection angle outside the overlap length is non-zero due to taking the fringing fields into account in the calculation.

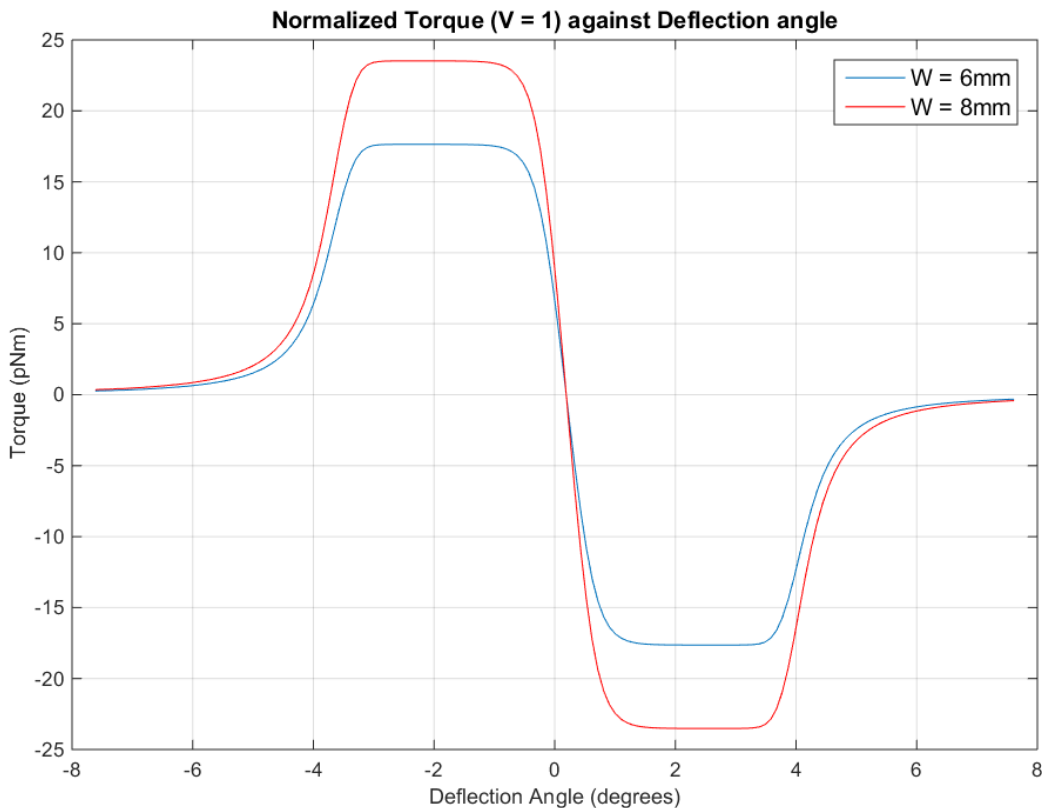


Figure 4.7: Graph of normalized Torque against deflection angle. The torque is normalized to the voltage whereby the Voltage is 1V.

This method of using the SC transform in calculating the force in MEMS devices has been used in [11,15,16]. [11,16] claim that the SC transformation method is almost as accurate as using FEA. Another method is described in [17] where an integration of the electric field obtained through the SC transformation can be used to determine Force. This method becomes complex and inaccurate when integrating around a corner of a polygon and hence was not used.

4.3 MATLAB Simulink Modelling

The MEMS mirror model in this project has been developed in MATLAB Simulink, which is a block diagram environment for simulation and model based design. The model was initially simulated in open loop whereby the drive voltage of the mirror was only time dependent and thereafter in closed loop where the drive voltage was made to be time and position dependent.

4.3.1 Simulink Model Creation

If we rearrange equation (4.1) to obtain equation (4.8), it can be represented as a block diagram as shown in Figure 4.8.

$$\ddot{\theta} = \frac{1}{I}(T - C\dot{\theta} - K\theta) \quad (4.8)$$

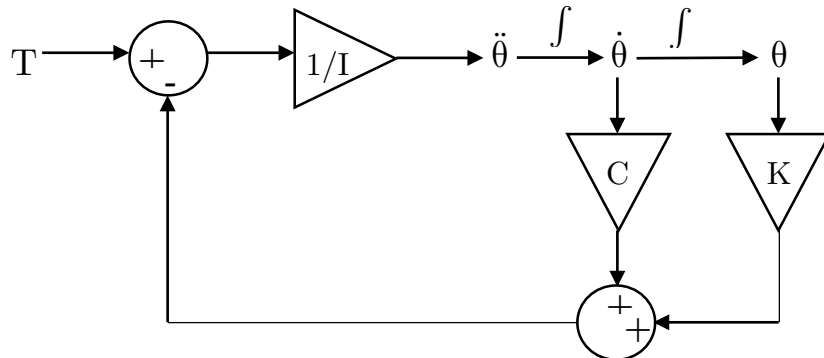


Figure 4.8: Block diagram representation of equation (4.8)

Using the above block diagram as reference, a Simulink model of the mirror was created and is shown below in Figure 4.9.

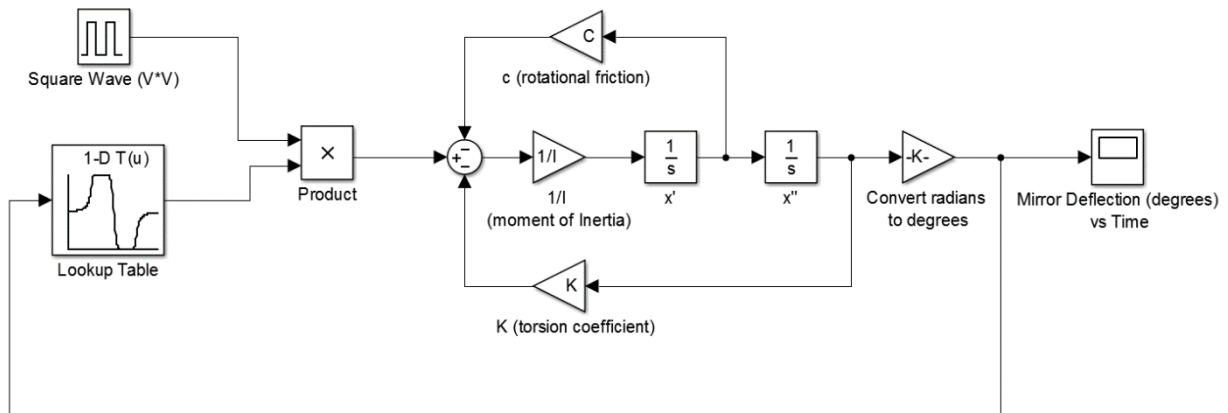


Figure 4.9: Simulink Block diagram representing the MEMS scanning mirror

The lookup table block outputs a normalized torque value corresponding to the mirror deflection in degrees. This is multiplied by the square of the drive voltage signal to obtain the Torque value and serves as the input to the model.

The drive voltage waveform is a square wave. Any another waveform could also be used but the choice of a square wave is for practical reasons. It is simpler and requires less circuitry to produce a high voltage square wave signal than another signal such as a high voltage sine-wave for example. This stems from the project requirement that the circuit footprint needs to be small.

4.3.2 Open Loop Simulation

The open loop simulations were performed with system parameters I , C and K calculated for a mirror with resonant frequency of 100Hz, Quality factor of 60 and mirror dimensions 17mm x 6mm. The simulation assumes that electrode arrays are along the full length of the device and that only one side of the electrodes of the mirror is being driven and the other side is used for capacitance sensing.

As the mirror oscillates, it goes through a maximum and minimum point in each cycle. At these points, there needs to be a positive transition in the drive voltage signal so that the electrostatic force tends to pull the mirror towards the centre point (also referred to as nominal position). When the mirror is at the nominal position, there needs to be a negative transition in the drive voltage signal, therefore removing the electrostatic force. The inertia of the mirror swings it in the direction of motion until it loses energy and at that point a positive transition in drive voltage is applied which pulls that mirror towards the nominal position again. Consequently, this is a square wave frequency at twice the frequency of mirror oscillation as shown in Figure 2.6. To achieve maximum amplitude, the square wave frequency should be at twice the resonant frequency of the mirror. As a starting point the square wave in the simulation was set up at 60V, 200Hz and a 50% duty cycle.

In open loop operation, there is no interdependency between the phase relationship of the square wave voltage and the mirror oscillation. This makes it difficult for the mirror to start up as the square wave could be out-of phase with the mirror leading to destructive interference and no significant oscillation. This was overcome by setting the square wave frequency at just above twice the resonant frequency at 204Hz and 25% duty cycle hence reducing the risk of destructive interference. Using this setting, the simulation was run at different voltage magnitudes and Figure 4.10 shows a plot of the deflection angle of the mirror as the voltage was swept.

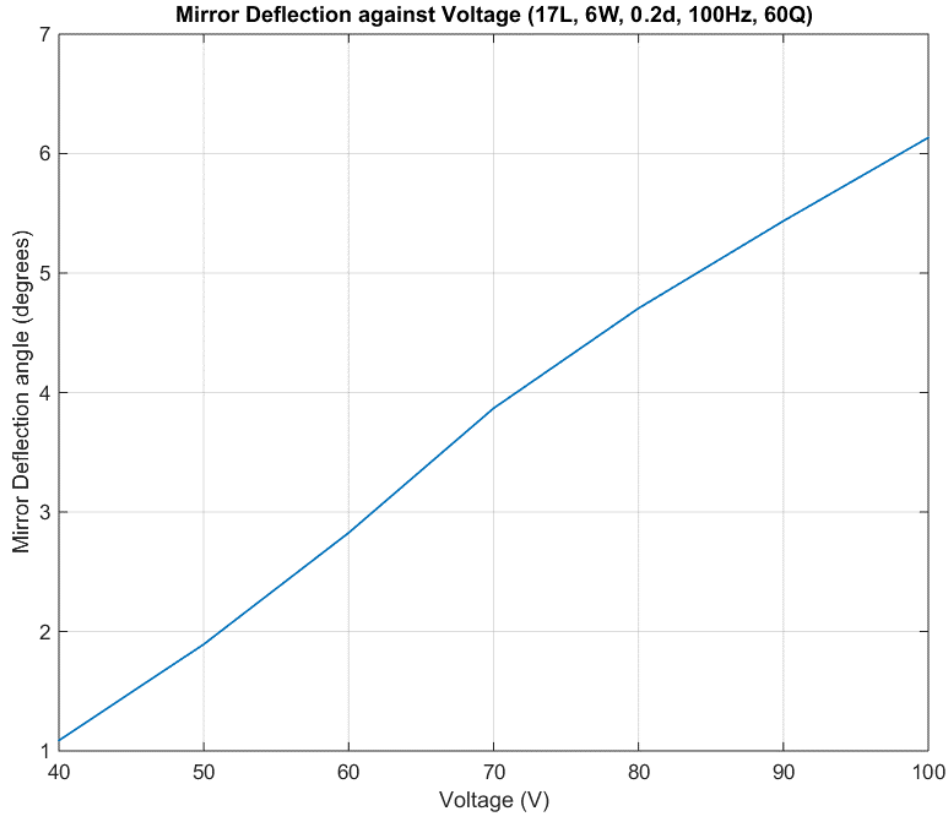


Figure 4.10: Graph of Mirror Deflection against voltage in open loop operation. The driving function was a square wave at 204Hz and 25% duty cycle. The mirror dimension was 17mm x 6mm, resonant frequency was 100Hz and the Quality Factor was 60.

The graph shows that as the voltage magnitude increases, the mirror deflection also increases. Mirror damping will also have an effect on the deflection angle and this is investigated in the closed loop simulation by varying the Quality factor of the mirror.

4.3.3 Closed Loop Simulation

In closed loop the transition of the square wave drive voltage is determined by the position of the mirror while it is oscillating. This means that the controller will need to sense the position of the mirror and drive it accordingly. The simulation assumes that the electrode arrays are along the full length of the device and that only one side of the electrodes of the mirror is being driven and the other side is used for capacitance sensing. For optimal operation, the drive signal should operate as shown in Figure 2.6.

From the open loop simulation, graphs of the mirror deflection and capacitance against time were plotted in Figure 4.11 to help in determining the control algorithm.

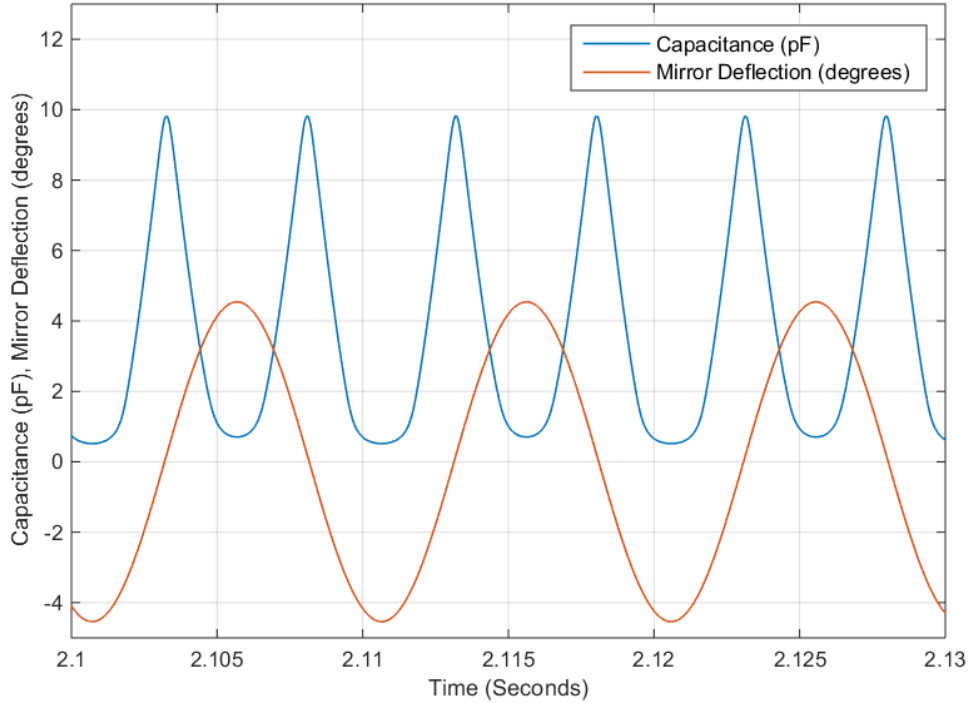


Figure 4.11: Graph of Mirror Deflection and corresponding electrode capacitance against time.

From observing the capacitance signal and comparing it to the mirror oscillation, for optimal operation in order to achieve maximum deflection, the drive signal needs to have a positive transition when the capacitance is maximum and a negative transition when capacitance is minimum. Differentiating the capacitance measurement signal can help in determining these points. If the derivative of the capacitance measurement crosses zero while it was rising, there needs to be positive transition in the drive signal or a negative transition if it was falling. This is the control algorithm needed to drive the mirror in closed loop.

In order to drive the mirror from rest, a start-up sequence is required before closed loop operation can run freely. This requires open loop operation for a short time before switching into closed loop. Changes to the Simulink model were made to add the closed loop operation. Additionally, since a digital platform is more likely to be used in the final electronic design of the controller, the step-size of the simulation was changed to obtain a sampling frequency of 10 kHz. Time delay was also added in the model to account for a finite measurement time of the capacitance measurement circuit. The new Simulink model is shown in Figure 4.12.

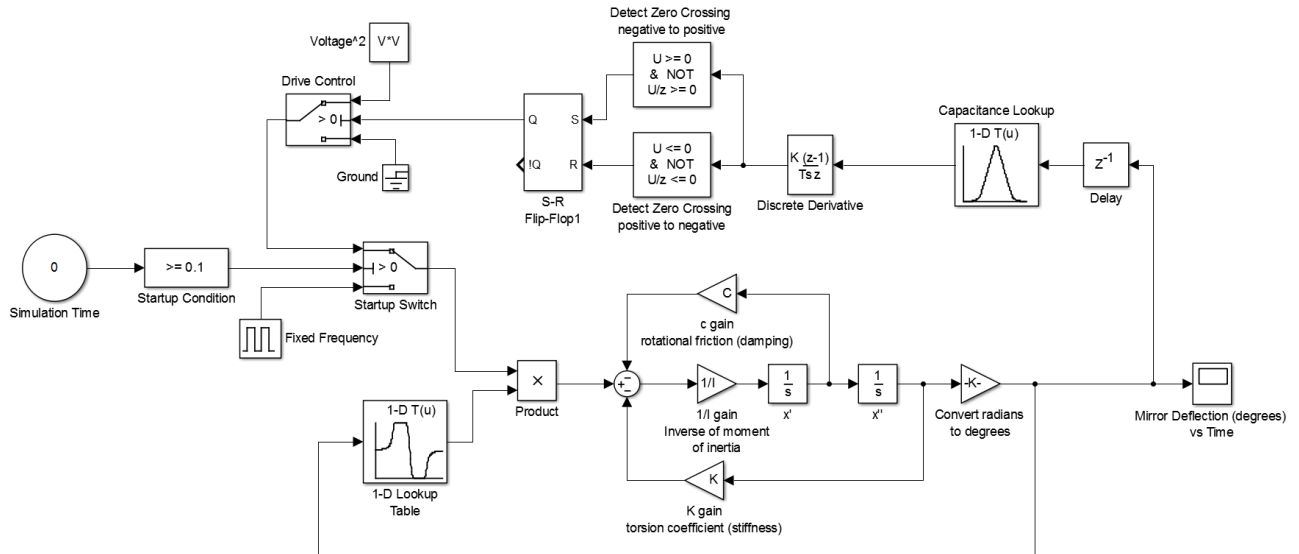


Figure 4.12: Simulink Model with Closed Loop Control

The mirror deflection was plotted against voltage magnitude as shown in Figure 4.13 at different Quality factors of the mirror at a resonant frequency of 100Hz.

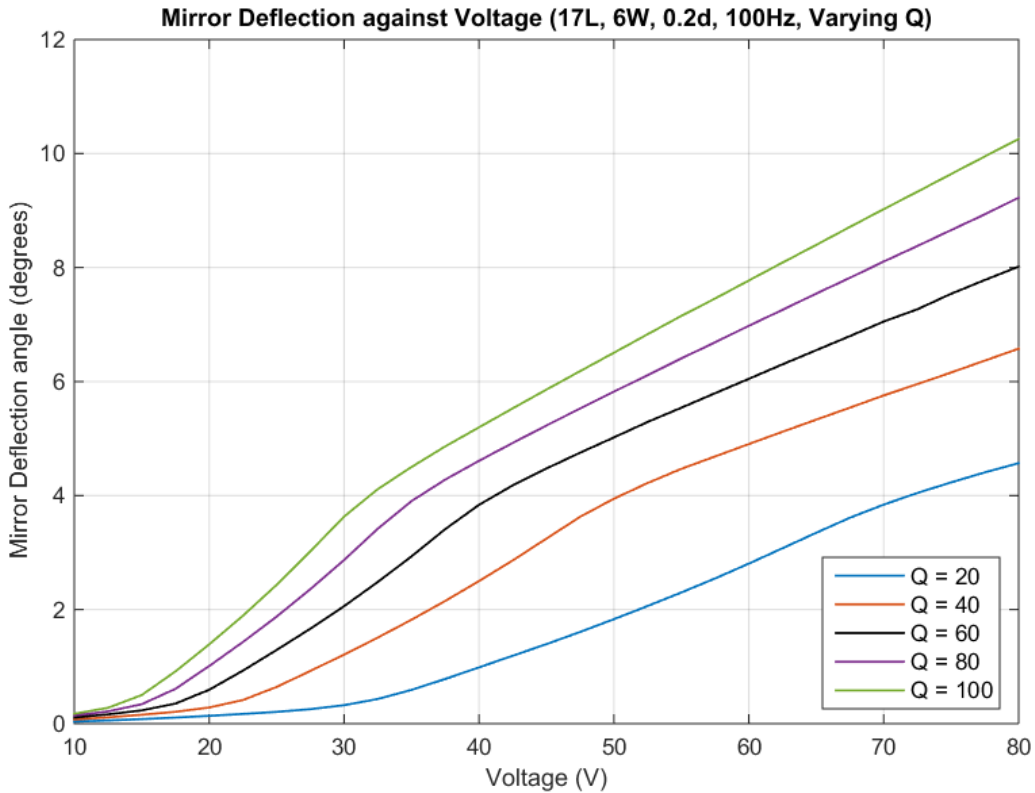


Figure 4.13: Graph of Mirror deflection against driving voltage under closed loop operation and simulation sampling frequency of 10 kHz.

The graph shows that as the voltage magnitude is increased, the mirror deflection also increases similar to the open loop case. Observing the plot carefully, the deflection angle increases linearly with the voltage above a mirror deflection of 4 degrees.

Additionally, since the system is in a discrete time domain, the sampling frequency has an influence on the mirror deflection angles. Figure 4.13 was obtained with a simulation sampling frequency at 10 kHz. Reducing this sampling frequency below 5 kHz causes the mirror deflection angle to reduce drastically at similar voltage magnitudes. This is because at lower sampling frequencies the drive signal transitions happen later than the optimum point, which reduces the mirror deflection.

Although the mirror can be driven in open loop, it requires the mirror resonant frequency to be known prior to the design of the driver. Due to the variance in resonant frequency because of manufacturing process variation and environmental factors, open loop operation is not practical. The simulation results in closed loop prove that it is viable to drive the mirror into resonance and hence this should be used to allow for variability in mirror properties.

The setup of the MATLAB simulation and appropriate toolboxes has been documented in the Appendix in section A.

5 Design

This section describes the circuit design of the driver from the high level design to more detailed explanations of the design decisions made. The description here is on the final design of the circuitry, however, at the end of the section there is some explanation given to justify and explain the differences from the initial circuit design.

5.1 High Level Design

The circuit design has 3 main aspects:

1. Capacitance Sensing to monitor position of the mirror
2. High Voltage (HV) DC-DC Converter to generate the square wave drive signal for the mirror
3. A Microcontroller to carry out the control algorithm to drive the mirror in closed loop

Figure 5.1 shows a high level system diagram of the driver and the connections between the MEMS mirror and the power source. Note that the MEMS scanning mirror has two electrode arrays on each of the lengths along the device. One is used for capacitance sensing while the other is used for driving the mirror.

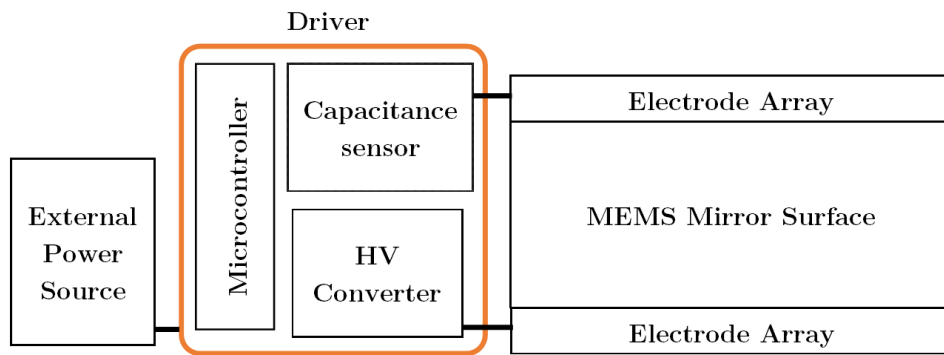


Figure 5.1: High level design block diagram showing interconnections between the different circuits and the MEMS mirror.

Some additional features are also required to fulfil the requirements of this project. These include:

- Adjustable Voltage Control of the HV Converter to allow amplitude control of mirror deflection to be controlled. This should be controllable via an input to the driver.
- A synchronisation signal output from the driver. This is needed to indicate mirror position to an external image source in order to synchronise the image source with the mirror oscillation.

5.2 High Voltage Converter Design

From the MATLAB simulation results, the mirror requires voltages in the range of 30-80V to achieve a mirror deflection of 5 degrees depending on the damping factor of the device. Since the mirror is to be used in head-up display applications, the power source is most likely to be a battery with a DC voltage of around 3-5V. This needs to be converted to a higher level in order to drive the mirror.

The chosen topology is a flyback converter design using an off-the shelf integrated circuit designed to charge photoflash capacitors in digital and film cameras to high voltages. The decision to use an off-the-shelf products helps in reducing the component count and therefore keeping the overall circuit footprint small as well. The chip used is an LT3468 and is particularly designed to use transformers with small footprints in the range of 6mm x 8mm making it ideal for this project. The recommended circuit from the datasheet [18] was modified as per the application note [19] to allow for adjustable output voltage control. The circuit was simulated and designed in a SPICE based software known as LTSpice. The circuit design is shown in Figure 5.2.

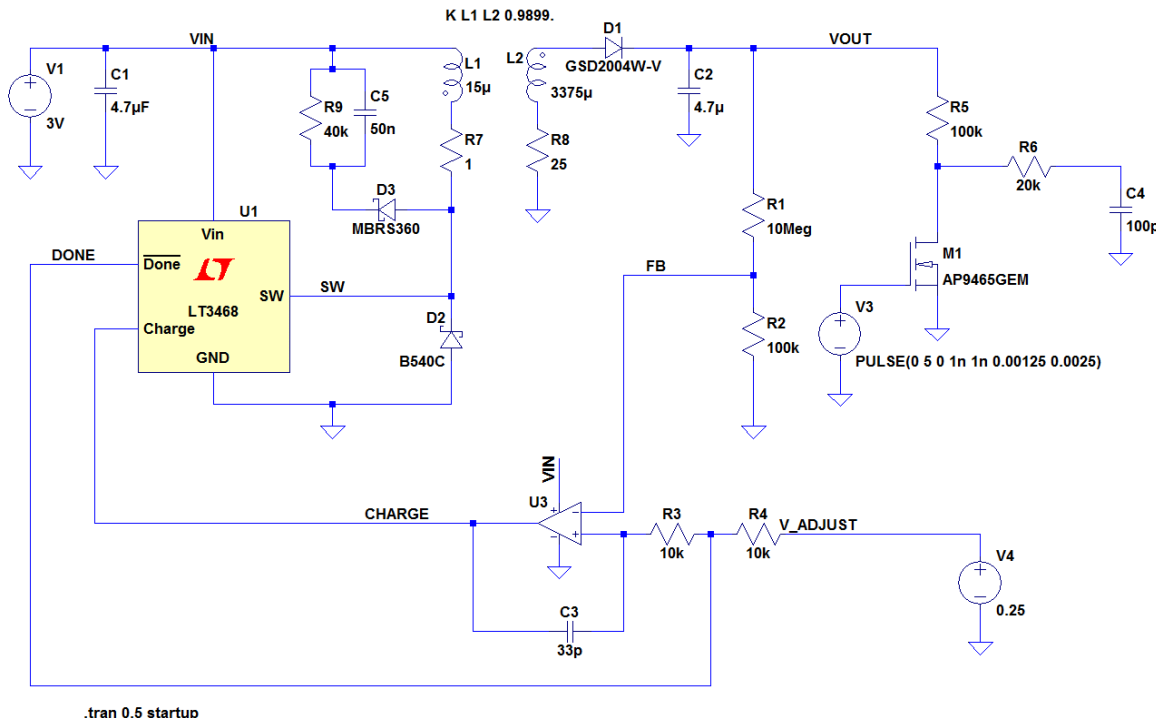


Figure 5.2: Flyback converter topology Circuit in LTSpice

The output voltage is regulated at a fixed voltage set by the transformer turns ratio. The CHARGE pin gives control of charging the output capacitor (C2) and the active low DONE pin indicates when the output capacitor has reached the target voltage. The output voltage

is automatically detected within the device through current sensing from the primary turn of the transformer.

Using these features, a control system can be added to adjust the output voltage as required. The Operational Amplifier (opamp), compares a ratio of the output with a reference input voltage (V_4). When the opamp inverting input exceeds the non-inverting input, the output of the opamp is low, which stops the charging of the output capacitor holding the voltage at the programmed input level. The CHARGE pin is held low until the output voltage drops low enough to trigger a high signal at the output voltage of the opamp and charge the output capacitor. In summary, the opamp generates a sequence of pulses to control the charging of the capacitor and consequently control the output voltage at the reference voltage (V_4). The feedback capacitor (C_3) provides AC hysteresis, sharpening the opamp output to prevent chattering at the trip point [19].

The output of the converter is connected to the MEMS mirror via an inverter switch (M_1) to control the square wave drive voltage transitions. C_4 is a 100pF capacitor used to model the MEMS mirror actuator since it is a capacitive load. R_5 and R_6 are placed in order to limit inrush current during switching transients. The gate of M_1 is connected to a pulse generator which is modelling a constant frequency mirror drive signal. When M_1 is off, the capacitive load will be charged but otherwise discharged. Therefore, it must be noted that the drive voltage is inverted with respect to the drive signal input to the gate of M_1 .

The components in the simulation have been selected based on calculation and availability. The output capacitor (C_2) needs to be a large value in the μF range to ensure low ripple voltage. An off-the-shelf flyback transformer with a ratio of 1:15 and primary side inductance of 15uH has been selected which gives a maximum output voltage of $\sim 330\text{V}$. This is modelled in LTSpice as two coupled inductors (L_1 and L_2). The feedback resistors (R_1 and R_2) should allow a scaling of the reference voltage such that 0-3.3V scales linearly with 0-330V for example, a reference voltage of 0.5V should give an output voltage of 50V. The resistors R_7 and R_8 have been placed to model the series resistance from the transformer windings as given by the maximum DC resistance from the datasheet [18]. The leakage inductance of the transformer is modelled using a coupling factor, k , which is related to the leakage inductance (L_{Leak}) by:

$$L_{Leak} = L(1 - k^2) \quad (5.1)$$

where L is the winding inductance. The maximum leakage inductance of the off-the-shelf transformer is $0.3\mu\text{H}$ in the primary winding. This gives a worst case coupling factor of $k = 0.9899$. Due to this leakage inductance, during switching of the internal switch in the LT3468, the voltage on the SW pin spikes above 40V and violates the maximum limit of

the voltage on that pin. Therefore, a snubber circuit is required such as the RCD clamp, which is a common snubber circuit used in flyback converters and is shown in the circuit as D3, R9 and C5.

The design of the snubber circuit was based on the notes in [20]. In summary, a large capacitor needs chosen to ensure a low ripple across it, $C_s \gg 1/f_s R_s$, where C_s is the snubber capacitance, f_s is the switching frequency and R_s is the snubber resistance. The voltage at the SW (V_{SW}) pin will rise until the power dissipated by R_s is equal to the average power transferred from the leakage inductance. This is given by:

$$\frac{V_{SW}^2}{R} = \frac{1}{2} L_{Leak} \cdot I_L^2 \cdot f_s \quad (5.2)$$

where I_L is the current through the primary transformer winding. Since the converter switching frequency is not fixed, it was found through simulation to be 34 kHz at a certain instant and this is used in the calculation along with the primary transformer current of 1.2A. If V_{SW} is limited to 20V, then we obtain $R_s = 40k\Omega$ and $C_s \gg 0.74nF$. These calculated values were simulated but the values chosen that yielded the best results in simulation were $R_s = 40k\Omega$ and $C_s = 50nF$. This limited the voltage on the switch pin to around 25V.

The efficiency of the converter was tested with a fixed 5mW load and resulted in an efficiency of approximately 76% at 70V output. However, as the output voltage was increased, the efficiency reduced to approximately 70% at 150V. Although adding the snubber circuit has helped with reducing stress on the SW pin of the chip, it also wastes some power. The average power dissipation from the snubber circuit calculated was $75.6\mu W$, therefore, it does not affect the efficiency significantly.

The plot in Figure 5.3 shows the ripple of the converter under simulation for an output voltage of 70V and a constant current load of 0.55mA. This shows that the ripple is approximately 100mV which is acceptable for the purpose of this project. Actual test results of the converter are discussed in section 5.5.



Figure 5.3: Output voltage ripple of the converter.

5.3 Capacitance Sensing Method

There are many capacitance sensing circuits that have already been developed and used in many applications. A common use is the capacitive touch sensing on touch-screen displays. In this project, small capacitance changes need to be measured at high measurement rates. These factors are the main limitations of all capacitance sensors. Another limitation in this project is the physical size of the circuitry and as a result the capacitance sensor needs to have a small footprint.

From the Schwarz-Christoffel transformation done in section 4.2, the capacitance change expected is approximately 10pF. The Simulink simulation also showed that relatively high sampling rates of higher than 5 kHz is required for optimal operation of the controller. Multiple papers were reviewed to study different sensor designs available. [21–25] use analogue techniques to measure the capacitance and require a lot of biasing and comprise of a large number of components which is not ideal in this project due to the size requirement. Most of these use a capacitive divider circuit whereby one of the capacitors is the varying capacitance. Additionally, [21], [23] and [25] use circuits which require very high frequency signals in the range of 5-10 MHz at approximately 10V peak-peak as inputs to the circuit. This is not realisable within the size requirement unless an external signal generator is used. [24] presents an interesting circuit but is designed for an integrated circuit and was therefore not pursued further. The method described in [26] uses a microcontroller to generate a high frequency square wave to charge and discharge the capacitor and measure the discharge time. This method was shown to be linear for capacitances in the range of 10pF to 100pF, however, the absolute error in the measurement was approximately 1pF which is too high for use in this project. [22] uses a charge based method which is shown to be able to measure capacitance changes in the femto farad range and could be adequate in this project. Although, some of the methods described in the papers could be used in the project, the best method would be an off-the-shelf product that guarantees capacitance resolution and high measuring rate. Some capacitance sensors such as the FD1004 [27] from Texas Instruments and AD7747 [28] from Analog Devices had the resolution needed but not the speed.

The chosen sensor is an off-the-shelf digital chip that can measure capacitances in the range from a few fF to hundreds of nF at upto 500 kHz measurement rates. It has a QFN32 package with a 5mm x 5mm footprint and requires very few passive components as biasing. The chip is manufactured by a German company known as “acam messelectronic gmbh” [29] specialising in time measurement devices. The capacitance sensor chip is known as the PICOCAP and uses accurate time measurements between the discharge time of a reference capacitor and a sense capacitor to determine the capacitance. The chip is ideal for this

project due to its small size and flexibility as it is programmable to the user's needs in terms of resolution, measuring rate and also interface method through a Standard Peripheral Interface (SPI), Inter-Integrated Circuit Bus (I²C) or even a pulse-coded generation output. Additionally, the datasheet of the device [30] lists MEMS sensors as one of the typical applications. The pulse coded generation outputs either a Pulse-Width-Modulated (PWM) signal or a Pulse-Density-Modulated (PDM) signal proportional to the capacitance measurement. These signals can be low pass filtered to obtain an analogue output signal.

5.4 Microcontroller

The following functions are required by the microcontroller:

- Analogue-to-Digital Converter (ADC): This is required if the capacitance measurement is to be captured via an analogue signal. It should have at least 10-bit resolution and a fast conversion time of less than 10 μ s to ensure high data sampling rates.
- Universal Asynchronous Receive Transmit (UART) Interface: This is used to interface with a computer for debugging and can be used for communication to the microcontroller to set variables such as the HV Converter voltage for amplitude control.
- SPI/I²C Interface: The PICOCAP capacitance sensor chip can be interfaced via an SPI or I²C bus to read in capacitance measurements into the microcontroller.
- Internal Timers: This allows the microcontroller to generate PWM output and also to generate interrupts based on time.
- General Purpose Input Output (GPIO) pins: These pins can be connected to various hardware circuits to be switched on and off.

The STM32F030xx family based on an ARM Cortex M0 microcontroller was chosen to be used on this project. One of the main reasons for the choice was due to familiarity with the development platform and availability of software drivers as well. It also has the necessary speed capability to perform sampling of data at higher rates than 10kHz due to its relatively high clock frequency at 48MHz and extremely fast ADC Conversion times.

Additionally, this family of microcontrollers is compatible with ARM's Real-Time-Operating-System (RTOS). This can allow simultaneous tasks to be run also results in better program management. Although not absolutely necessary, the RTOS can be useful to seamlessly run tasks in parallel such as running the control algorithm and at the same time communicating with a computer for data transfer via UART.

5.5 Differences from Initial Design

The initial design of the circuits was manufactured on a PCB and tested. The results of the testing of the initial circuitry contributed towards the final design that is documented previously in this section.

In the initial version of the HV Converter, the transformer used was large (22mm x 16mm) and did not require a snubber circuit as its leakage inductance was quite low. To ensure that the final PCB size was within the footprint specified by the project requirements, the transformer size needed to be reduced. A small transformer was designed and wound by hand but resulted in very high leakage inductance. In addition, a hand-wound transformer is not ideal for mass-manufacturability due to variance in its properties. Consequently a much smaller off-the shelf transformer was found and used in the final design (See Figure 5.4). This required a snubber circuit as described in section 5.2 to ensure voltage limits were not violated.

Similarly, the microcontroller also needed to change. The initial microcontroller chosen was an ATMEL ATTiny 841 based on the popularity of the ATTiny devices by hobbyists and their low-power consumption. However, there are two main reasons as to why this microcontroller was not appropriate for this project:

1. The ADC in the microcontroller has a reported conversion time of $1\mu s$, which is fast enough for the purpose of this project. However, after detailed reading of the datasheet, fast conversions are only possible if less than 10bit resolution is acceptable. To achieve the full 10-bit resolution required, the ADC clock needs to run at 125 kHz which increases the conversion time to $120\mu s$. If the capacitance is measured using an analogue signal, the ADC in this microcontroller is too slow to achieve high enough signal sampling rates and yet leave time for executing other code.
2. The maximum clock speed was 8MHz if no external clock is provided. To ensure fast interfacing and data transfer through the SPI interface to the PICOCAP chip, the clock speed needs to be higher.

Figure 5.4 shows an annotated picture of the initial PCB made along with the sizes of the replacement components. Using these new components and placing components on both sides of the PCB, it is possible to fit all the circuitry on a package size of 50mm x 25mm as required in this project.

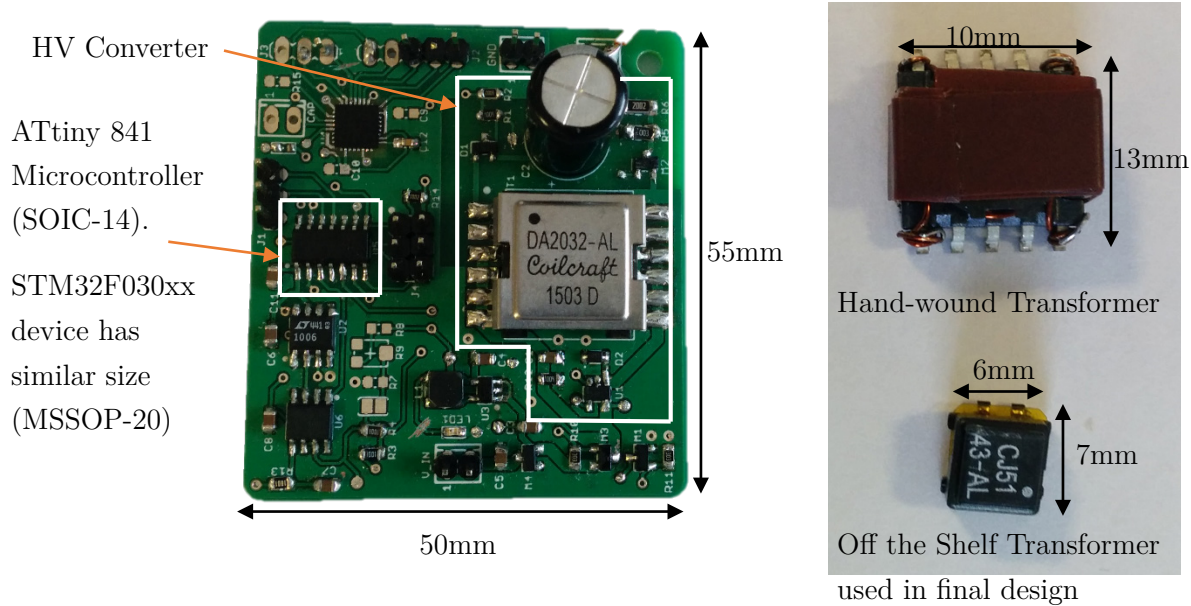


Figure 5.4: Annotated picture of the Initial PCB designed and sizes of different transformers tested on the HV Converter.

6 Implementation

This section describes the implementation of the final circuitry and the microcontroller software. There is detailed descriptions on the testing of the individual circuits, in particular the HV converter and the Capacitance sensor chip. A full circuit diagram can be seen In Appendix B.

6.1 HV Converter

The HV converter circuit implemented is shown in Figure 5.2. To allow software control of the output voltage, the reference voltage of the HV converter is derived from a low-pass-filtered PWM signal originating from the microcontroller. The tests were performed with a constant 110pF capacitive load to simulate the similar load expected from the mirror.

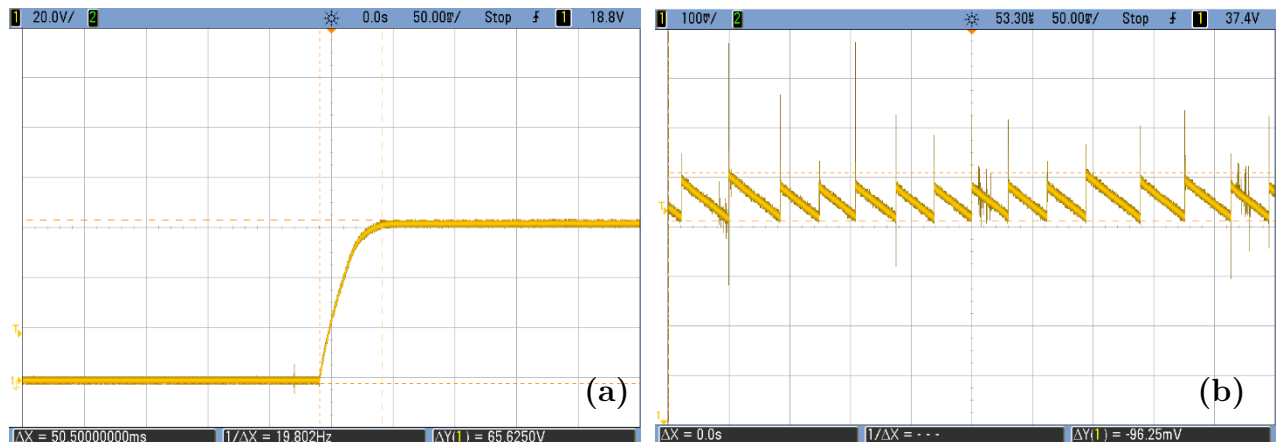


Figure 6.1: Oscilloscope Captures of the Output voltage of the HV Converter. (a): The start-up time of the converter to get to a target voltage of 60V. (b): Output voltage ripple of the converter.

Figure 22(a) shows the HV converter output voltage during startup from 0V to 60V. There is no overshoot and the settling time is approximately 50ms. Figure 6.1(b) shows the output voltage ripple of the converter, which is approximately 85mV and is similar to the SPICE simulation results.

In the simulation, the output capacitor of the HV converter had a value of $4.7\mu F$. In the circuit under test, the output capacitor was a 250V, $22\mu F$ aluminium electrolytic capacitor. This capacitor is quite large in terms of its size (10mm diameter and 20mm height) and has been changed in the final implementation to a ceramic type that has a maximum height of 1.65mm. To accommodate for a higher voltage rating, four ceramic capacitors each of $15\mu F$ and 100V rating have been wired in a series and parallel combination to achieve a voltage rating on the combined output capacitor of 200V and a value of $15\mu F$. Although, the

maximum voltage required is probably lower than 100V, some voltage headroom is needed on the capacitor to ensure long lifetime. Additionally, to ensure that the voltage across each series connected capacitor is the same, two resistors with $10M\Omega$ value have been wired in parallel with the series connected capacitors. This can be seen in the circuit schematic in Appendix B.

The inverter switch at the output of the converter was also tested to observe the rise and fall times on the capacitive load as shown in Figure 6.2.

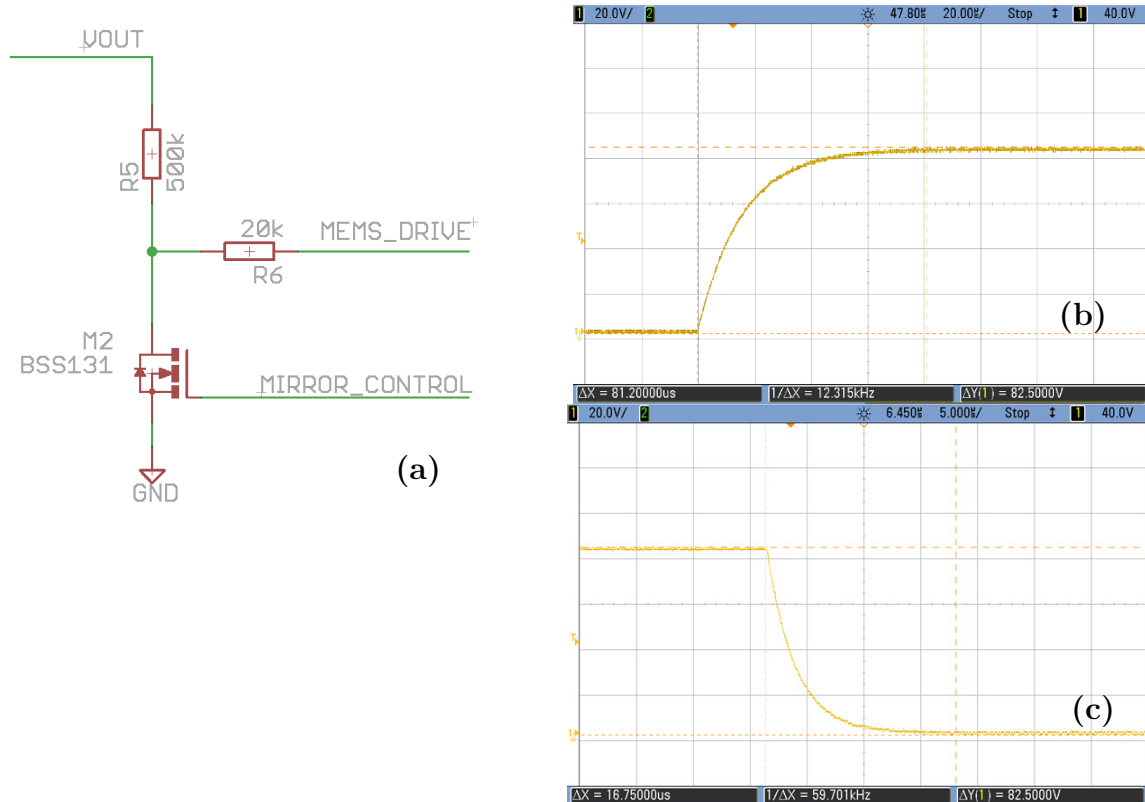


Figure 6.2: Output inverter switch testing. (a): Circuit diagram of the inverter switch. (b): Rise time of the voltage measured at the load when switch M2 is switched off (c): Fall time of voltage at the load when switch M2 is switched on.

The results show a rise time of $81\mu\text{s}$ and a fall time of $16.75\mu\text{s}$ when the converter voltage is set to 80V. This is fast enough to produce a high voltage sharp square wave at a frequency of around 200 Hz.

The voltage on the SW pin on the controller chip was also tested and the result showed that the voltage was limited to approximately 35V as shown in Figure 6.3. This is less than 50V which is the maximum voltage limit of the pin.

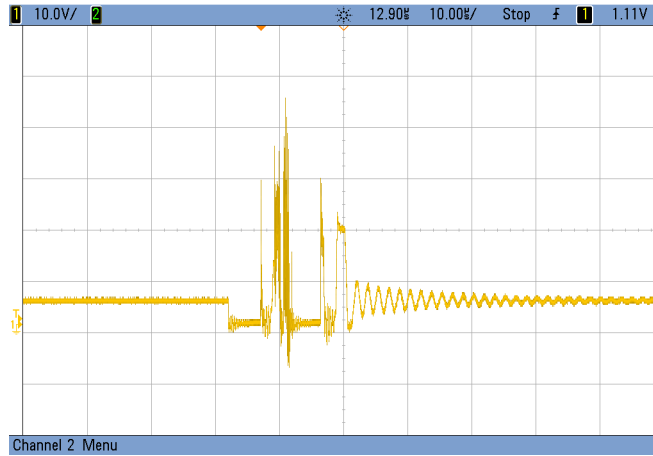


Figure 6.3: Voltage on the SW pin of the HV Converter.

6.2 Capacitance Sensor

The Capacitance sensor used is the PICOCAP device manufactured by a German company named “acam messelectronic gmbh”. The sensor works by charging the sense capacitor to the supply voltage and then discharging it through a fixed resistor. The discharge time is measured against a reference capacitor and a capacitance ratio is calculated simply by using the two time measurements and dividing them. Due to the accurate time measurement available on the chip, very short charge and discharge times for the capacitors can be programmed to obtain extremely fast measuring rates of up to 500 kHz.

For the setup used in this project, the measuring rate achieved was 16.7 kHz implying that a new conversion is completed every $60\ \mu s$. The closed loop MATLAB simulation demonstrated that high sampling frequencies of above 5 kHz are required in order to obtain optimum deflection angles and therefore, this chip is adequate for the purpose.

The capacitance measurement was tested with high tolerance ($\pm 2.5\%$) static capacitors available in the lab. The measurement was done using an internal 31pF reference capacitor. Table 6.1 shows the capacitance ratio measured for different capacitors sensed.

Table 6.1: Measured Capacitance Ratio.

Capacitance Value (C_{Value})	Capacitance Ratio ($C_{Ratio} = C_{Value}/C_{REF}$)
68pF	0.768
78pF	1.83
90pF	3.07
115pF	5.46

By plotting a graph of the capacitance ratio against capacitance value from Table 6.1, it can be seen that the sensor is linear but is scaled and offset. A straight line equation of the graph obtained from Table 6.1 is given by:

$$C_{Ratio} = 0.00995 \cdot C_{Value} - 5.9531 \quad (6.1)$$

The offset and gain error can be due to different discharge resistors used for the reference capacitor and sense capacitor. Another reason could be that the internal capacitor selected as reference is not exactly 31pF. However, since the sensor is linear, we can scale it in software if needed.

The noise on the sensor reading was measured to be approximately 18fF giving a signal-to-noise ratio (SNR) of 9 bits if a range of 10pF is assumed. These measurements were made using the evaluation kit together with the evaluation software provided by the manufacturer.

Microcontroller interfacing to the chip can be done through SPI or I²C. In the I²C protocol, the data transfer speed can limit the capacitance measuring rate, therefore SPI is preferred since it operates at higher clock frequencies and allows faster data transfer. In this project, the SPI interface should be used due to the high measurement rates required. However, the interface could not be established between the microcontroller and the PICOCAP chip. As an alternative, the chip provides a PDM/PWM output which can be low-pass-filtered to obtain a purely analogue signal proportional to the capacitance measured. This can be attached to an ADC pin of the microcontroller to sense the capacitance.

The PDM output has been used in this project, which can be scaled such that 0 -100% modulation represents a certain range of capacitance.

6.3 Software

The microcontroller software has been written using ARM's Microcontroller Development Kit (MDK) with ARM's C/C++ compiler in the Keil uVision5 Integrated Development Environment (IDE). This is a licensed paid for IDE however, a free version has been used in this project which limits the program size to 32 kB.

6.3.1 ADC Setup

The ADC in the microcontroller is used to read the analogue capacitance value. This is done through the Direct-Memory-Access (DMA) controller setup in a continuous conversion mode. This allows the ADC to continuously sample the analogue signal and store it in a circular buffer of user specified size at a certain memory address. The ADC values can then be read by the microcontroller by reading the values in the memory addresses of the circular buffer. This allows the ADCs to run in the background with no software intervention until

the instant at which the value is required, therefore reducing processor overhead. Additionally, the values in the buffer can easily be averaged in software to filter the noise in the signal.

Each ADC conversion takes $1.5\mu s$ in this microcontroller. Consequently, the ADC buffer size has been chosen to be 50. At the instant, when the buffer is read, it is averaged; therefore, the result is effectively an average value of the analogue signal based on the $75\mu s$ prior to reading the buffer.

6.3.2 Control Algorithm

From the simulation in 4.3.3, a 10 kHz sampling frequency was shown to be adequate to drive the mirror with reasonable amplitudes. This sampling frequency is setup using an interrupt in software to sample the ADC buffer every $100\mu s$.

In simple terms, the control algorithm is a peak and trough detector which aims to perform an action based on whether a peak or a trough in a signal is detected. The flowchart in Figure 26 below helps explain the algorithm.

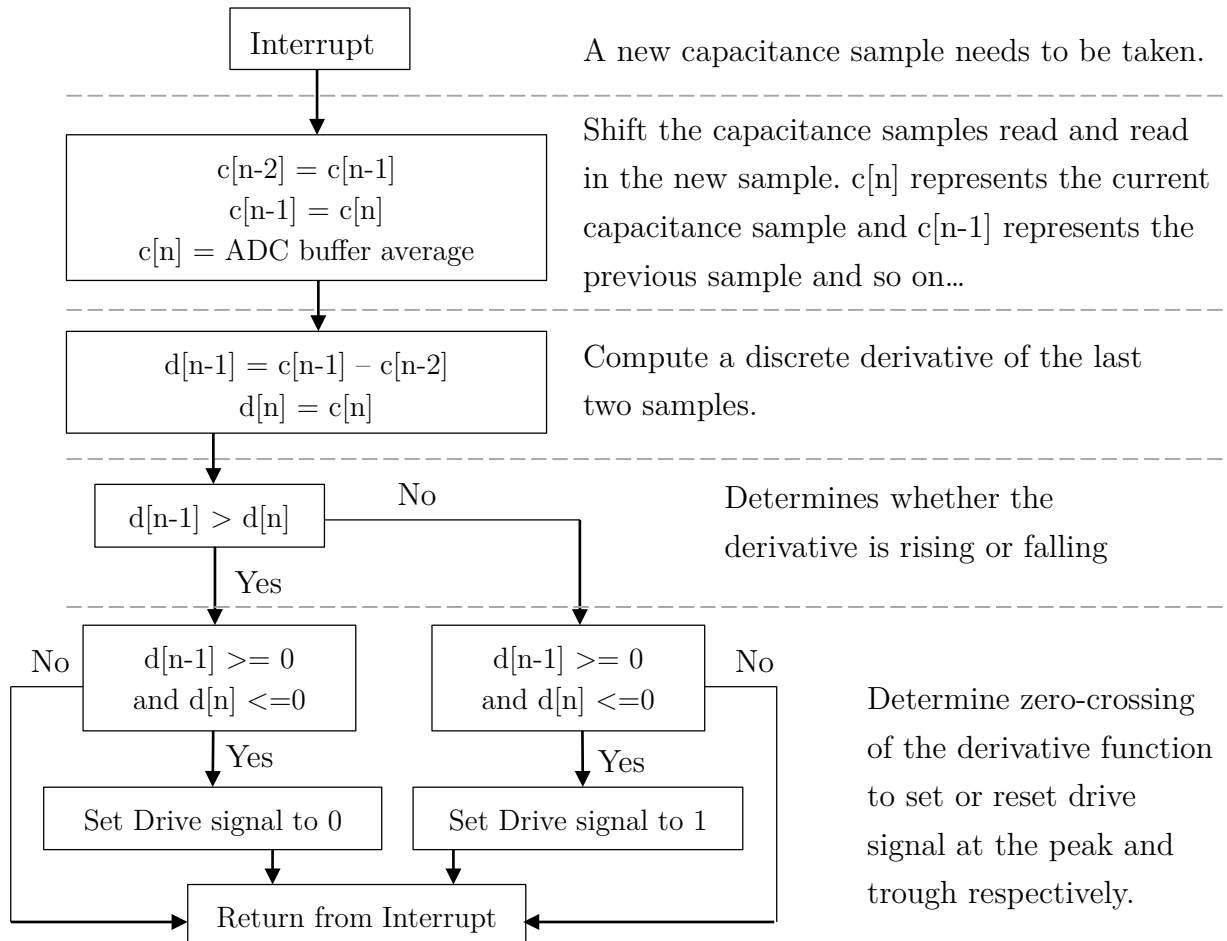


Figure 6.4: Control Algorithm Flow diagram

Note that the computation of the discrete derivative does not involve the division of the time difference between the samples. Since the interrupt is happening once every $100\mu s$, the time between samples can be assumed to be constant. Therefore, the computed derivative is scaled version of the actual derivative and is performed faster since floating point divisions can take more time to perform in the processor.

Due to noise on the capacitance signal and transient coupling from the drive side to the sense side during switching of the high voltage, there needs to be dead band period where no measurements are taken immediately after transactions in the drive signal. This has been done by setting a flag that pauses the interrupts and delays the processor for a period of time equal to the dead band period before resetting the flag, re-enabling interrupts and continuing with the algorithm.

In order to test this algorithm, a function generator was used to input a 100Hz periodic signal into the ADC pin of the microcontroller to mimic a capacitance change to see if the peaks and troughs would be detected. Figure 6.5 shows oscilloscope captures showing the algorithm working for both a sine wave and a triangle wave.

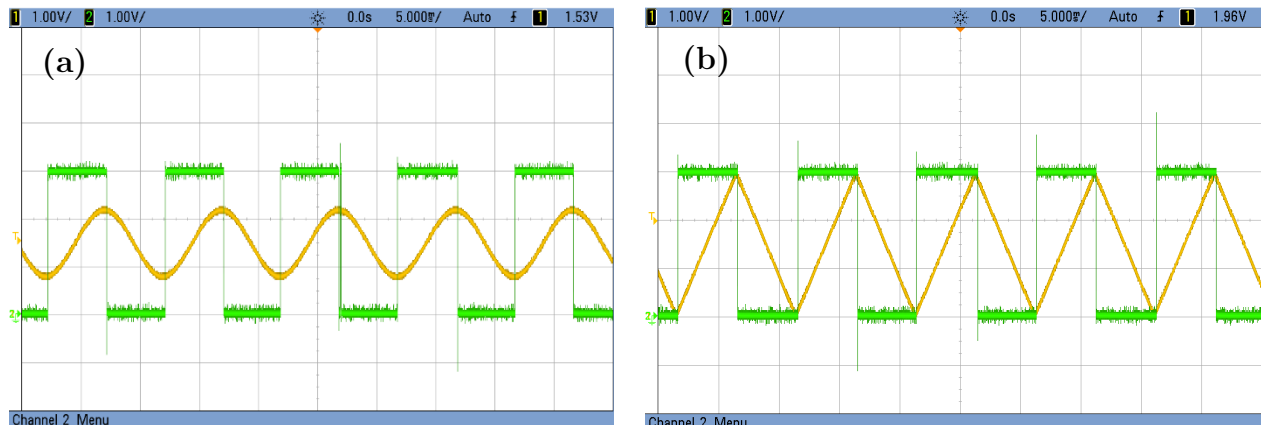


Figure 6.5: Algorithm testing. Yellow signal is the input to the ADC from a function generator and the green signal is the output from the microcontroller which changes when a peak or trough is detected. (a): Testing using a sine wave as input. (b): Testing using a triangle wave as input.

The algorithm also includes a start-up sequence that drives the mirror at a fixed frequency for a short period of time to start it oscillating and then switches over to the closed loop controller.

6.3.3 RTX RTOS

The ARM RTX RTOS has been used to concurrently run different tasks in parallel. This is done by time division multiplexing of the system resources. This allows the software to be easier to write when there are multiple tasks that need to be run.

In this project, the RTOS is used to run two tasks. One that constantly runs the control algorithm (main task) and another that is used for data transfer (auxillary task) via UART to allow external digital control of the HV Converter voltage to control mirror deflection amplitude. Although an analogue input to the driver circuit could suffice in adjusting the HV converter output, it is much safer to use the digital control. This is because the code can be written to ensure that the voltage limit of the converter is not exceed even when the external control signal demands a higher output voltage from the converter.

Additionally, the decision to use a separate task for data transfer can also be used to communicate the mirror position digitally via UART. Another benefit of using the RTOS is the ability to write the software for modulation of the imaging LEDs on the same microcontroller but simply on a separate task that the RTOS will handle. Therefore, the microcontroller can potentially be used for the control of both the driver circuit and the imaging as well, however, this is beyond the scope of this project.

6.3.4 PC Interfacing and Serial Debugging

For debugging purposes, the UART interface of the microcontroller was connected to a computer using a USB FTDI TTL-232R Cable. Data transfer was done via a virtual COM port on the computer. A python application Graphical User Interface (GUI) shown in Figure 6.6 was written to test the data transfer to and from the microcontroller via the UART interface.

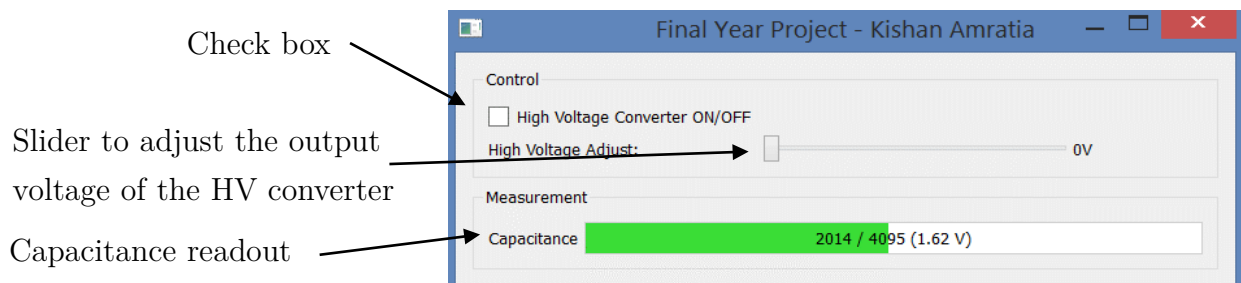


Figure 6.6: Python GUI Application on a computer that interfaces with the microcontroller UART interface for transfer data

This is done on the axillary task on the microcontroller, where it looks for any changes in the data received from the computer and also sends the capacitance data to the computer for updating the bar in the capacitance readout. Additional functions for communication to the microcontroller can easily be added to this.

6.4 Final Printed Circuit Board

6.4.1 Input Protection and Power Circuitry

The final circuit requires a voltage regulator, some switches and some protection circuitry in addition to the capacitance sensor, microcontroller and the HV Converter. Figure 6.7 shows the circuit schematic of this additional circuitry. The power input to the system is through a 2-way power connector which is connected straight to a reverse polarity protection MOSFET, M4. This is done due to prior experience whereby the supply voltage reversal has led to damaging results to the circuitry. The MOSFET is rated appropriately to ensure that it can handle the surge currents required by the rest of the circuitry and has a low on-state resistance to ensure minimal power loss in the MOSFET. A 3.3V voltage regulator is used to power the microcontroller and the capacitance sensor. The chosen device was a linear regulator, LM3480 that can output a maximum of 100mA. The HV converter on/off switch allows the input to the HV converter to be switched on and off.

The rating of the devices in the circuit gives a power input voltage range between 5V to 16V. Anything voltage below 5V may not be regulated to 3.3V exactly and anything above 16V can break some of the chips. The maximum reverse voltage that can be put into the device is -20V.

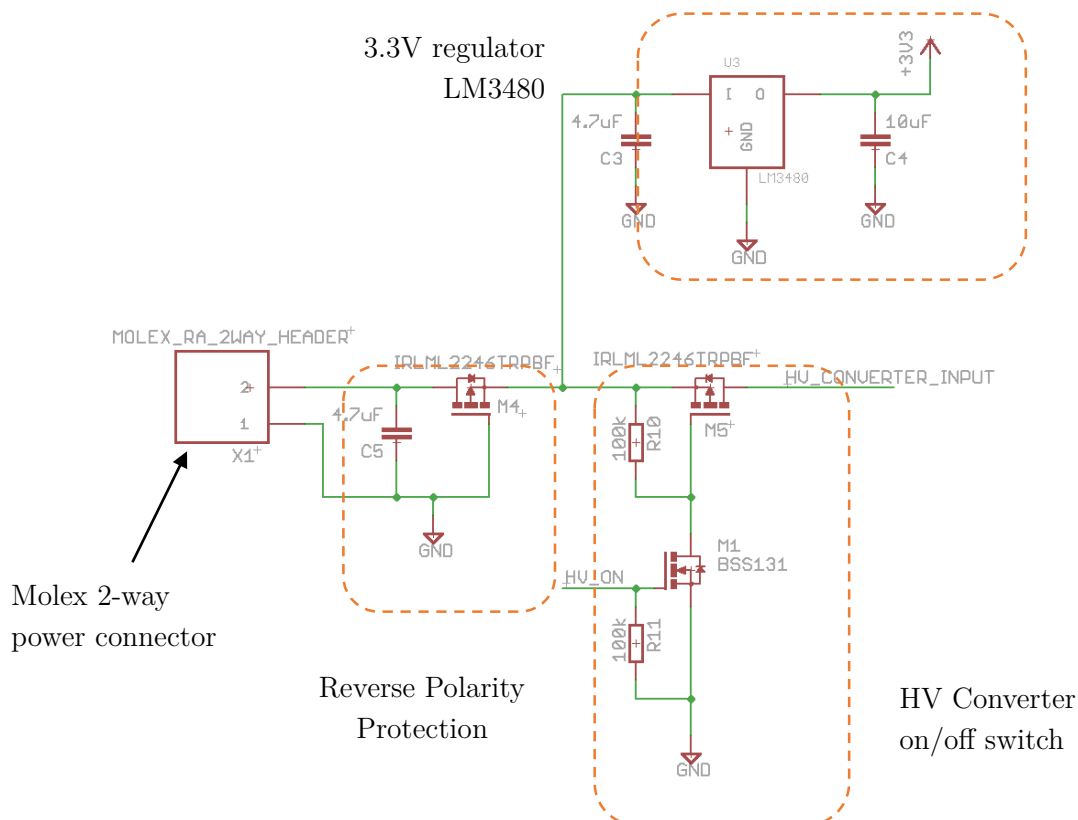


Figure 6.7: Annotated circuit diagram of the power input stage showing the reverse polarity protection, HV Converter switch and the 3.3V regulator.

6.4.2 PCB Design and Size

The project requires the footprint of the overall circuitry to be within 50mm x 25mm. In order to fit all the circuitry on this footprint, a double sided PCB can be used. However, due to the density of the circuitry, it is very difficult and probably not possible to route the PCB with a standard 2-layer board. Therefore, a 4-layer board is required in order to route all the components.

By using the free version of EAGLE, 4-layer routing is not possible. As a result, the final PCB design was made by sandwiching two 2-layer boards but ensuring that the footprint was kept at 50mm x 25mm with a height of less than 10mm between the boards. Having two boards sandwiched has its own benefits such as separation of the power circuitry and the HV Converter from the microcontroller and the capacitance sensor. However, it also has drawbacks which is an increase in manufacturing cost due to having 2 boards, although it could be comparable to the cost of a single 4-layer board.

External connections to the PCB are provided through 0.5mm pitch FPC connectors.

Testing of the mirror was done very late in the project timeframe due to delays in fabrication. As a result, the final board could not be manufactured due to time constraints but has been designed and shown to fit within the footprint required as shown in Figure 6.8.

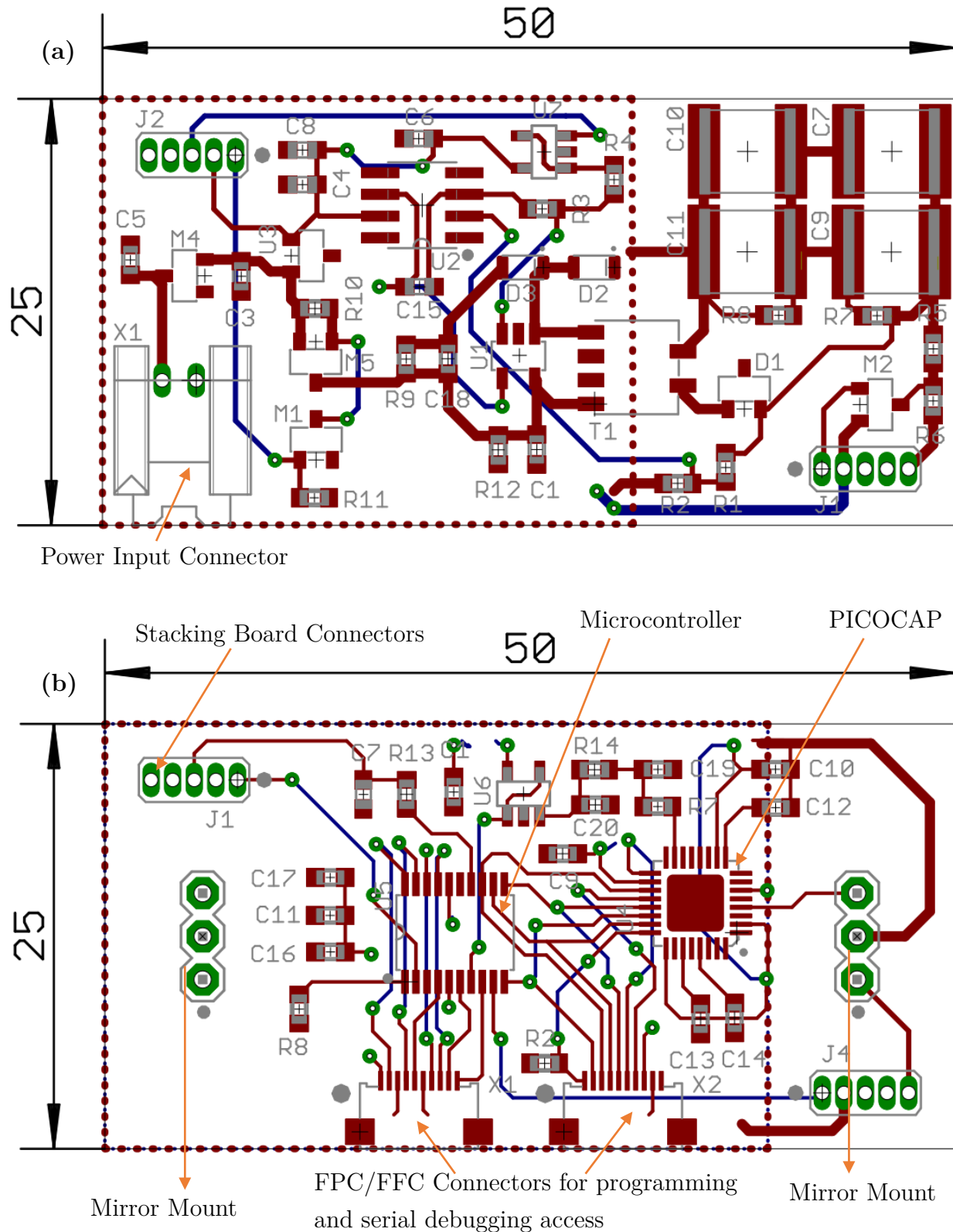


Figure 6.8: PCB Designs (Dimensions in mm) of the two stacked boards. (a): Voltage Converter board containing the HV Converter. (b): Digital board containing the microcontroller, capacitance sensor, connectors for external signals and the mirror mounts.

7 Testing and Results

This section discusses the results from testing of the full driver circuit together with a prototype scanning mirror.

7.1 Test Setup

Since the mirror can be oscillating at a relatively high frequency that cannot be detected by the human eye, a laser beam deflection onto a screen can be used to measure the mirror deflection. If the laser beam is displayed as a line on the screen after being deflected, it proves that the mirror is oscillating. This setup is shown in the pictures in Figure 7.1.

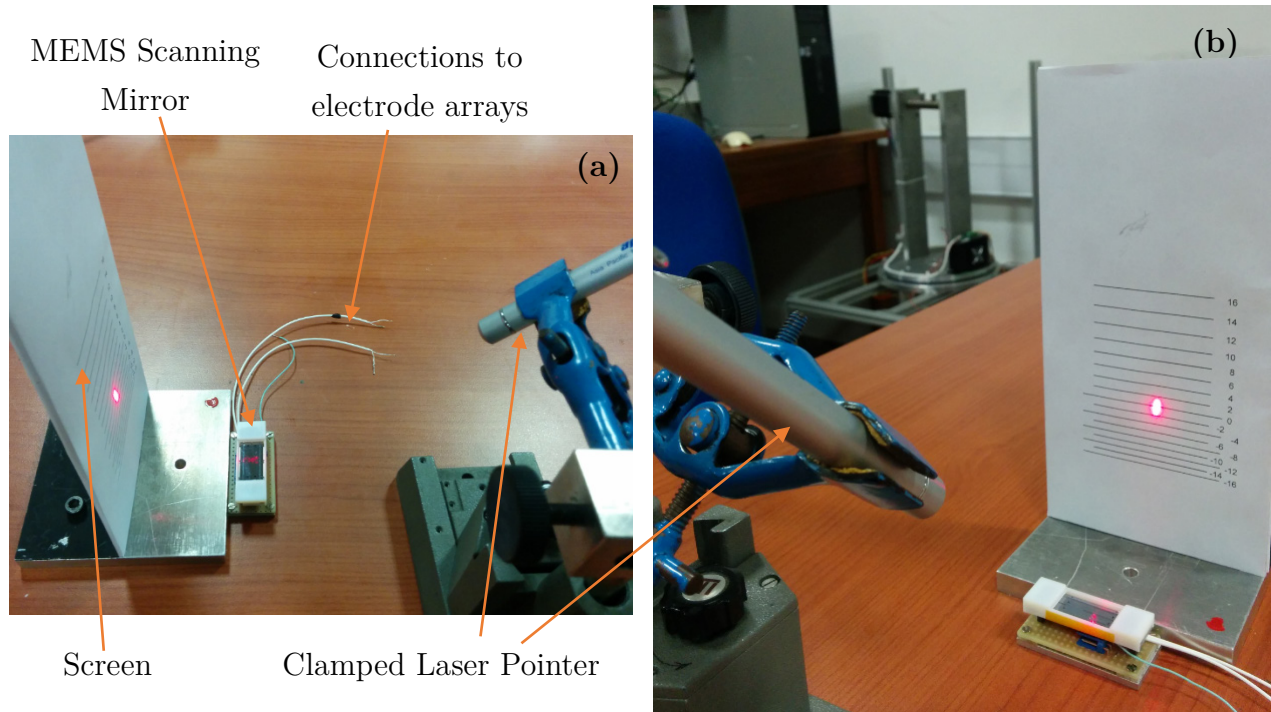


Figure 7.1: Test setup where a laser beam is reflected onto the screen of a static mirror.

(a): Top view of the setup. (b): View of the setup from behind the laser.

The screen has lines on to help in measuring the beam deflection. The lines are spaced such that the beam deflection corresponds to the mirror deflection angle. The marks range from -16 to +16 which corresponds to a mirror deflection angle of -8 degrees to 8 degrees. To calibrate the setup, the laser pointer must be set at 45 degrees to the mirror surface such that the reflection of the beam hits the screen at the 0 degrees mark.

7.2 Open Loop Tests

The open loop tests were performed by driving the mirror single sided using a fixed voltage but varying the frequency of a square wave drive signal using a function generator.

7.2.1 Mirror Properties and Transient Coupling

Due to over-etching in the fabrication process, the mirror resonant frequency was lower than 100Hz. The over-etching affected the electrode array in terms of the dimensions of the electrodes. This means that the change in capacitance and the torque is bound to be lower than expected from the calculations done in section 4.2.

Figure 7.2 is an equivalent circuit for the MEMS scanning mirror. This can be used to explain capacitive coupling between the drive and sense side electrodes.

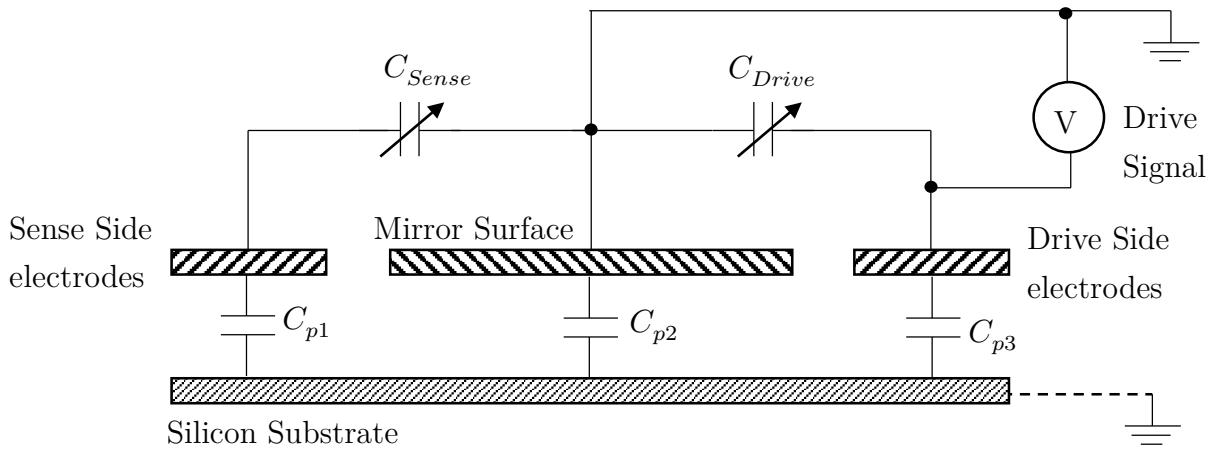


Figure 7.2: MEMS Scanning Mirror Equivalent Circuit from a side view of the mirror showing the different layers in the silicon

The C_{Sense} and C_{Drive} are variable capacitances that change as the mirror oscillates. C_{p1} , C_{p2} and C_{p3} are parasitic capacitances to the bottom silicon substrate layer in the device with the dielectric being a $4\mu m$ silicon-dioxide (SiO_2) layer. If the substrate is not grounded, at switching events of the drive signal, there could be some transient voltage coupling from C_{p3} to C_{p1} and into the sense side electrodes which could cause the capacitance measurement at the sense side to be wrong just after the switching instant. However, if the substrate is tied to ground potential, C_{p2} is eliminated and thereby reducing the transient coupling seen at the sense side. Figure 7.3 shows oscilloscope captures of the transient coupling on the sense side on the real mirror during switching events for both scenarios where the substrate is not grounded and when it is. It clearly shows that the transient coupling is indeed lower when grounding the substrate and hence experiments were performed with the substrate grounded at all times.

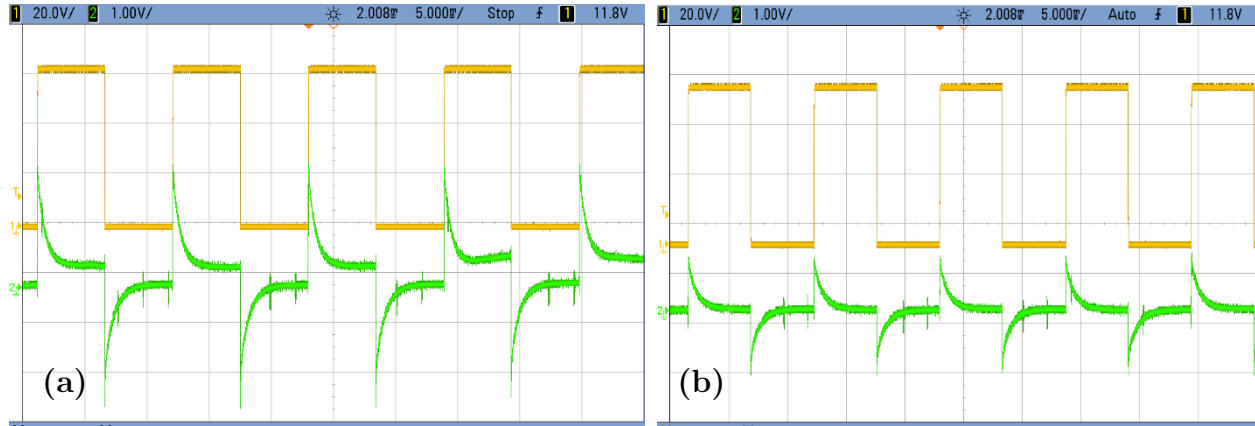


Figure 7.3: Transient capacitive coupling from the drive side to the sense side on the real mirror. (a): When substrate is not grounded. (b): When substrate is grounded.

The static capacitance of the electrodes was also measured using an LCR meter. The measured value includes the coaxial cable capacitance connected to the electrode arrays:
 Sense Electrode Array Capacitance: 66.7pF
 Drive Electrode Array Capacitance: 65.8pF

7.2.2 Resonant Frequency

In order to find the resonant frequency of the mirror, it was driven in open loop. The test setup described in 7.1 was used while the driving voltage was fixed at 60V and the frequency was varied with a fixed 50% duty cycle. The resonant frequency was found to be at 45.7 Hz. This was done by increasing the frequency until the laser beam starting showing a line on the screen at approximately 53 Hz. As the frequency was reduced at increments of 0.1 Hz, the line amplitude increased indicating that the mirror was being driven ever so close to resonance at every increment. At 45.6Hz, the scan line of the laser beam broke down into a point, which signified that the resonant frequency was at **45.7 Hz**. Figure 7.4 shows the laser beam scanned onto the screen in the test setup while being driven in open loop.

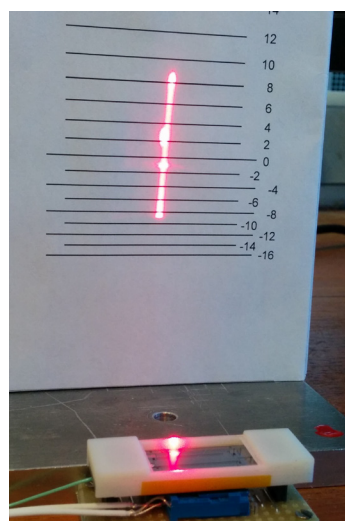


Figure 7.4: Image showing the laser beam scanning vertically along the screen

7.2.3 Test Results

The open loop tests were done at a driving signal at twice the resonant frequency at 25% (Figure 7.5) and 50% (Figure 7.6) duty cycle while varying the voltage amplitude of the HV Converter. The mirror deflection was measured using the laser beam deflection on the screen.

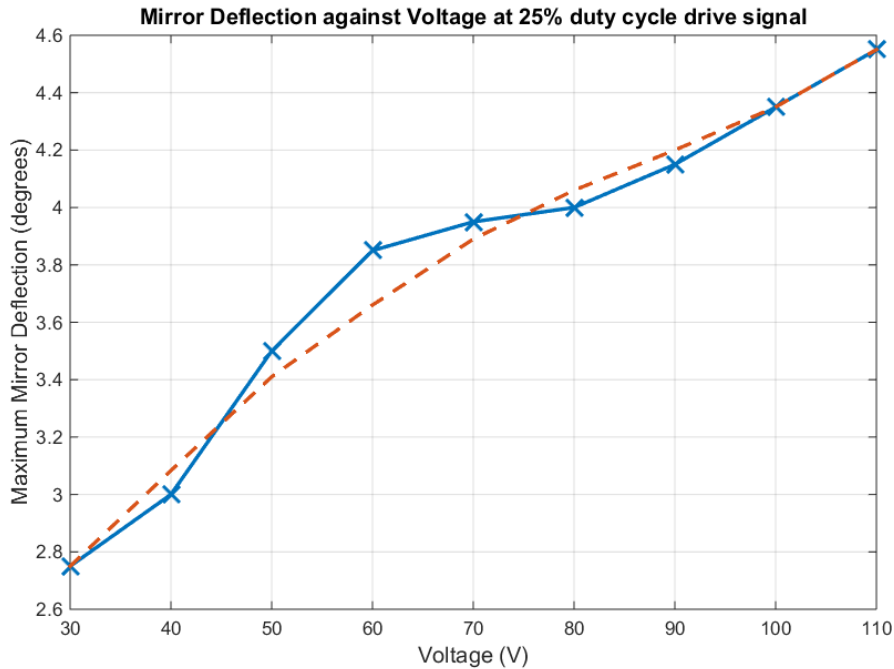


Figure 7.5: Graph of Mirror deflection against voltage with a 25% duty cycle drive signal

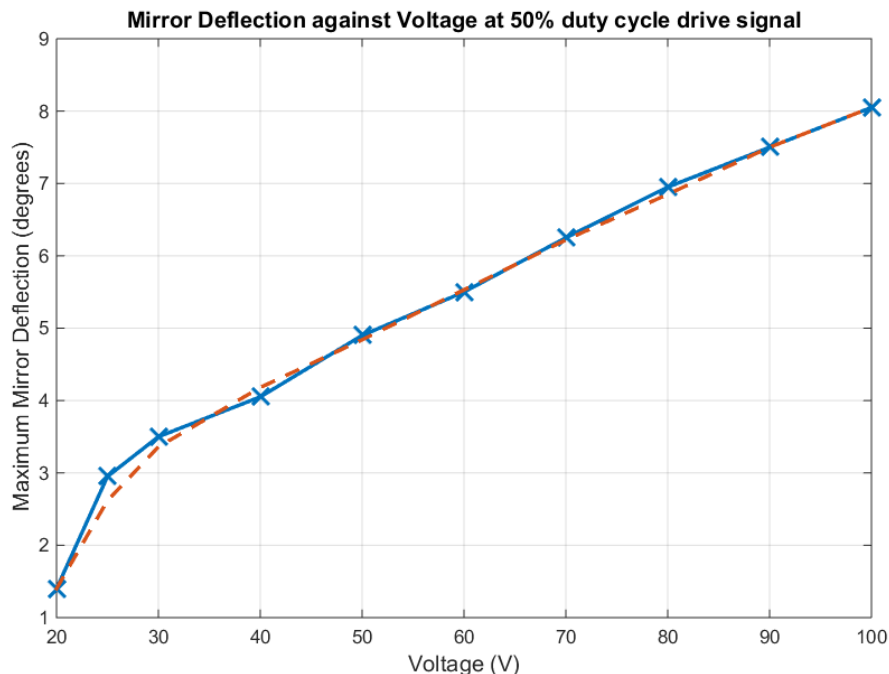


Figure 7.6: Graph of Mirror deflection against voltage with a 50% duty cycle drive signal

Since the measurement of the laser beam deflection was done by eye, there is some measurement error. In both graphs, an average best fit curve has also been plotted in a red dashed line. It is clear and expected that the mirror deflection is lower at 25% duty cycle than at 50% and as the voltage is increased, the mirror deflection also increases. Following these tests, similar tests are done in the closed loop scenario in section 7.3 and compared against the simulation results.

7.2.4 Phase Delay and Capacitance Measurement

During the open loop tests, the output of the capacitance sensor was measured and displayed alongside the drive signal on the oscilloscope. This showed that the 2nd order filter to filter the PDM signal from the capacitance sensor chip introduced a phase shift in the actual signal. This was deduced from the edges of the square wave driving signal not matching the peaks and troughs of the capacitance signal indicating that there is a significant phase shift in the signal. The phase delay was measured by measuring the time difference between the peak of the capacitance signal and a falling edge of the drive signal. This was found to be approximately 3.8ms which can be seen in Figure 7.7.

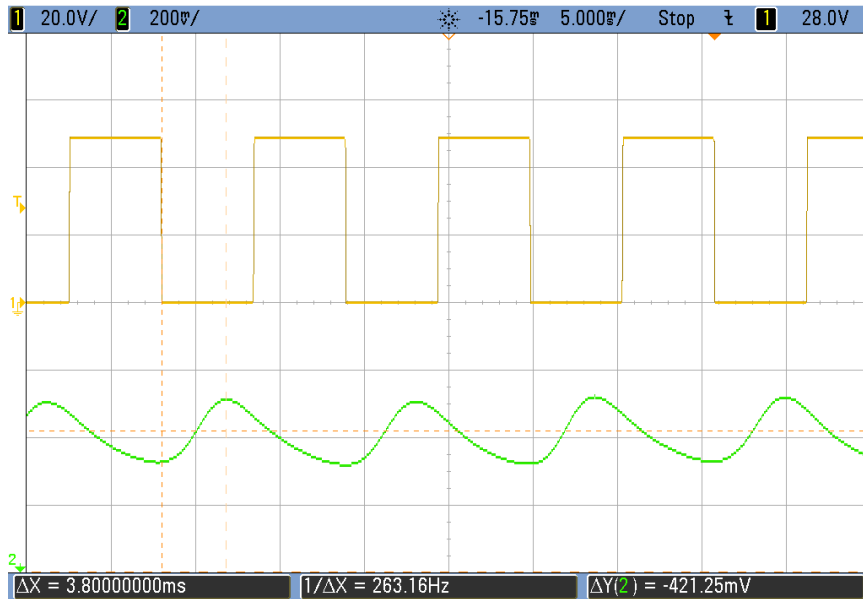


Figure 7.7: Oscilloscope Capture showing the drive signal at 50V, 91.5Hz at 50% duty cycle (yellow trace). The capacitance signal (green trace) has been averaged in the oscilloscope to remove the noise and show the signal clearly.

From the capacitance measurement signal, the value is between 62pF and 66.5pF giving a capacitance range of 4.5pF as the mirror is oscillating. This is much smaller than expected from the simulation but can be explained by the over-etching in the fabrication process.

7.3 Closed Loop Tests

7.3.1 Control Algorithm Testing and Phase Delay Compensation

After realising that there is some phase delay in the signal, it needed to be compensated in software such that the action on the signal occurs exactly one cycle later than when measured. This is done in software by adding a delay between when a peak or trough is detected and when the drive transition occurs, whereby the software delay is equal to the phase delay.

To start the mirror oscillating, it was driven at a fixed frequency for a short period of time and then switched over to closed loop control. This was at 100Hz at 25% duty cycle.

7.3.2 Test Results

Test results were recorded by adjusting the voltage and measuring the beam deflection on the screen. Some jitter in the oscillation was observed that caused the laser beam scan line on the screen to oscillate its amplitude; therefore, it was difficult to capture the results. Also, the jitter was more notable at higher voltage magnitudes. Figure 7.8 shows a graph of the results. An average best fit curve has also been plotted as a red dashed line.

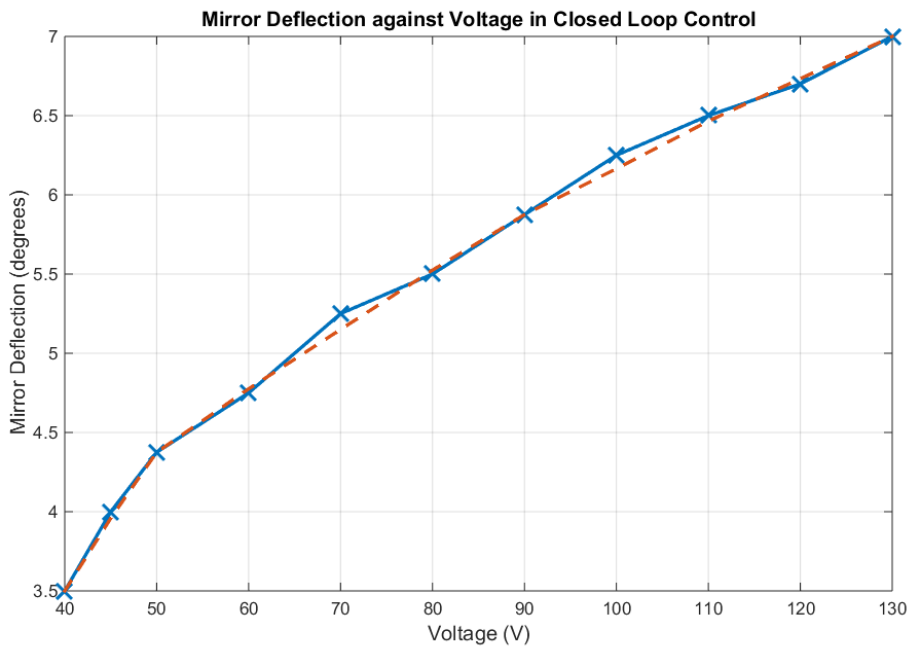


Figure 7.8: Graph of Mirror deflection against voltage in closed loop control

Since the mirror deflection in the closed loop graph is lower than in open loop, it suggests that the negative drive voltage transitions aren't precisely at the zero-crossings of the mirror and likewise the positive transitions aren't at the maximum and minimum points of the

mirror. Therefore, when comparing the simulation results in section 7.4, the closed loop simulation results is compared with the open loop test shown in Figure 7.6 as these are likely to be the closest match to optimum control achieved in the simulations.

To reduce jitter, the control algorithm was adjusted so that there is only square wave pulse for every cycle of oscillation instead of two. This reduced the jitter but at the expense of reducing the mirror deflection angle.

The aim of the hardware implemented in this was to achieve closed loop control of the mirror oscillation through capacitance sensing and generation of suitable excitation signals to the actuators. This has been demonstrated to work but with sub-optimal operation whereby there is jitter in the mirror oscillation. This could not be improved upon due to the short time available for testing and experimentation with the prototype scanning mirror. Methods of improving this have been documented in the Future Work in section 9.3.

7.4 Comparison with Simulation Results

Bearing in mind that the real mirror is slightly different from the mirror properties in the simulations, the simulation was done again with more realistic mirror parameters assumed:

- Dimensions: 17mm x 8mm
- Resonant Frequency: 45.7 Hz
- The initial simulation assumed that the electrode array is along the full length of the device. In reality, the array is 90% of the length of the device (at 15.3 mm) and therefore reducing the number of gaps in the comb drive.
- Additionally, due to the over-etching in the fabrication process, the electrodes are much smaller than designed for. According to the capacitance measurement, the change is approximately 4.5pF when running in open loop. The width the electrodes was adjusted while keeping the pitch (width + gap) at $50\mu m$ to try and achieve a capacitance range of 4.5pF. The geometry to achieve this is $w = 20\mu m$ and $g = 30\mu m$.

Figure 7.9 shows a graph of mirror deflection against voltage from the closed loop simulation overlaid with the open loop experimental results at 50% duty cycle. Although this comparison can seem inappropriate, as explained in section 7.3.2, the closed loop experimental results show a lower amplitude than the open loop experimental results suggesting that the closed loop controller is not optimal. Therefore, it is a closer match to compare the closed loop simulation result to the open loop experimental result.

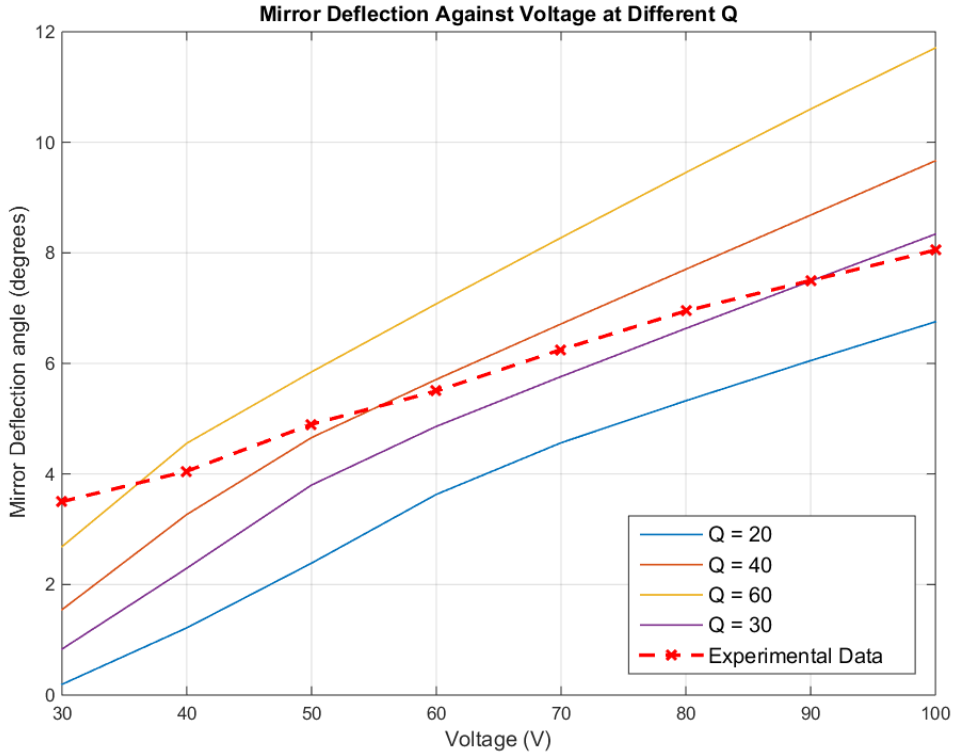


Figure 7.9: Comparison of closed loop simulation with open loop experimental data.

Figure 7.9 shows that the mirror deflection increases with the voltage as expected but the gradient of the curve isn't the same. In order to quantify the error, a mean-squared error (MSE) was used to compare the experimental data against the simulation results. Table 7.1 shows the mean-squared error for different simulated Q values of the mirror.

Table 7.1: Mean-squared-error of the experimental result compared to the simulation result at different Q simulated.

Q	MSE
20	4.7543
30	1.5301
32	1.2677
35	1.0721
37	1.0514
40	1.1664
45	1.6482
50	2.4430
60	4.7114

From this table, the Q of the mirror cannot be accurately determined since the parameters of the mirror are not exactly known but an estimate can be made. The lowest MSE occurs between Q of 30 and 40, therefore, it can be expected to be anywhere between this range.

Through observation, some of the trends in the simulation graphs are similar to the experimental results. An example is that the mirror deflection in the experimental results becomes linear around the 4 degree deflection angle mark, which is evident in Figure 7.5 and Figure 7.7 and similar to the simulation results.

8 Project Evaluation

The project has been evaluated in two parts. The Simulation model has been evaluated by comparing the simulation results against the experimental data and the hardware has been evaluated in terms of the achievement and drawbacks and including the limitations faced.

8.1 Simulation Model Evaluation

The first basis of evaluation of the model is the accuracy and realistic nature of it. Since the magnitudes of the simulation results and experimental results are of the same order, the model can be declared as realistic. On the other hand, since the actual mirror specifications are different from the planned design due to over-etching in fabrication and that the actual parameters and dimensions of the mirror cannot be measured, the absolute accuracy of the model cannot be determined. However, calculating a correlation coefficient (r) between the experimental data and the simulation results can help quantify the trend. The r was calculated for the simulation with the lowest MSE ($Q = 37$) against the experimental data, resulting in $r = 0.9949$, which is very high. Therefore, based on the results being of the same order of magnitude and following the same trend it can be concluded that the model is able to capture the key characteristics of the mirror.

8.2 Hardware Evaluation

All the hardware components implemented in this project have been shown to work. However, there are some minor drawbacks. As a result of not being able to interface the capacitance chip via SPI in due time, the capacitance measurement signal was based on a low-pass filtered PDM signal which had a large phase delay associated with it. This required software compensation, which is not ideal.

The inappropriate microcontroller selection in the initial stages of the hardware development wasted a lot of time in developing the firmware for it. In the end, it turned out to be obsolete. However, it was a learning experience both in terms writing firmware for that type of microcontroller and in terms of overlooking the details in the datasheet, therefore it is a mistake to learn from. On the other hand, the new microcontroller selected has the required capability to perform the control algorithm and other functions simultaneously due to the RTOS.

The initial plan for the hardware was to have it manufactured on a PCB with a particular footprint of 50mm x 25mm. All circuitry for the driver has been demonstrated to fit within the footprint but requires either a single 4-layer PCB or two stacked 2-layer PCBs. In terms

of cost, a single 4-layer board would be less expensive and would also occupy less volume, thereby being the better option. However, in this project, two stacked 2-layer boards were designed since the software tools for 4-layer routing was not available.

Due to delays in the fabrication of the mirror beyond the control of this project, extensive hardware testing and experimentation using the prototype mirror was not possible. Therefore many improvements after realisations from the testing such as jitter reduction algorithms were not implemented due to the time available. However, closed loop control was demonstrated as per the objectives of this project and the proposed improvements documented briefly in the Future Work section of this report.

9 Future Work

Some of the improvements that can be made in the future is documented in this section.

9.1 Other Capacitance Measurement Circuits

Although not necessarily required, the capacitance measurement circuit in [22] could possibly be used as an alternative to the digital chip to improve the resolution and range. This may increase the size of the circuitry due to the increase in the number of components but using smaller Surface-Mount-Device (SMD) packages could help reduce the size.

9.2 SPI Interfacing

The SPI interface between the capacitance sensor chip and the microcontroller could not be established. As a result an analogue signal was used to determine the capacitance from the sensor, which had significant phase delay. To avoid having to compensate for the phase delay in software, it is better to get the SPI interface working.

9.3 Improved Control Algorithms to Reduce Jitter

The jitter is caused by constant changes in the drive frequency. An improved algorithm could utilize averaging the frequency found from detecting the capacitance peaks and locking the drive frequency at a moving average of the frequency calculated from peak detection. This could still include jitter if the frequency jumps around.

A full-proof method could be to sweep the frequencies until the frequency that maximizes the capacitance range is found. The algorithm should then lock the driving frequency at the frequency found that maximizes the capacitance range. Theoretically, this should work as it is similar to finding the resonant frequency using a function generator as the drive signal source. The capacitance measurement is then used as a feedback signal to check and ensure that the mirror is indeed oscillating. If the oscillation breaks down, the capacitance measurement could be used to detect this and restart the controller.

10 Conclusion

As MEMS mirrors are more widely adopted into head-up-display and micro projection applications, the use of large scanning mirrors is still uncommon, especially when compared to commercial development. This project has produced a simulation model for a large area silicon MEMS scanning mirror that has been shown to capture the key characteristics of the mirror when compared to actual experimental data. As a result, the model has the potential to be used as a verification tool in the future when designing MEMS scanning mirrors.

The project also involved the development of an optimised driver for the mirror. This is a closed loop controller, which uses capacitance sensing to determine mirror position and generates appropriate excitation signals. The closed loop control of the system was achieved but with jitter in the oscillation. Future work on algorithm improvements have been proposed to reduce jitter.

In conclusion, the project has been successful in terms of developing the simulation model and the driver hardware. Although a final PCB could not be manufactured, the system has been demonstrated to work in closed loop operation and a PCB within the size requirement has been designed. With some improvements to the control algorithm, the work in this project can be taken one step further into developing an imaging system to use alongside the MEMS scanning mirror and the driver. This can then be prototyped in a head-up-display as per the original intended use for the mirror.

Bibliography

1. Riordan M. The lost history of the transistor. *IEEE Spectr.* 2004;41(5).
2. Petersen KE. Silicon as a Mechanical Material. *Proceedings of the IEEE.* 1982. p. 420–57.
3. Bean KE. Anisotropic etching of silicon. *IEEE Trans Electron Devices.* 1978;25(10).
4. Liu C. Foundations of MEMS. 2005. 1-19 p.
5. Krijnen G, Tas N. Micromechanical Actuators [Internet]. Enschede, The Netherlands; Available from: http://www.utwente.nl/ewi/tst/education/elbach/mandt/extra/background/mems_actuators.pdf
6. Madou M, Gurtner C. Bio-MEMS - the impact of MEMS on biotechnology in the 21st century. *60th DRC Conf Dig Device Res Conf.* 2002;
7. Ziaie B, Baldi A, Lei M, Gu Y, Siegel RA. Hard and soft micromachining for BioMEMS: Review of techniques and examples of applications in microfluidics and drug delivery. *Advanced Drug Delivery Reviews.* 2004. p. 145–72.
8. Ekinci KL, Roukes ML. Nanoelectromechanical systems. *Rev Sci Instrum.* 2005;76(6).
9. Holmstrom STS, Baran U, Urey H. MEMS Laser Scanners: A Review. *J Microelectromechanical Syst.* 2014;23(2):259–75.
10. Holmes A. Out-Of-Plane Comb Drive Analysis. Personal Communication.
11. Li F. Online Capacitance Modeling Tool for Conductors Represented as Simply-Connected Polygonal Geometries in 2D. *J Sens Technol.* 2012;02(03):155–63.
12. Driscoll T a. Algorithm 756; a MATLAB toolbox for Schwarz-Christoffel mapping. *ACM Trans Math Softw.* 1996;22(2):168–86.
13. Riley KKF, Hobson MP, Bence SJ. Mathematical Methods for Physics and Engineering. 2006. 843 p.
14. Driscoll T a. Schwarz-Christoffel toolbox user's guide. 1994;26. Available from: <http://ecommons.library.cornell.edu/handle/1813/6204>

15. Bruschi P, Nannini A, Pieri F, Raffa G, Vigna B, Zerbini S. Electrostatic analysis of a comb-finger actuator with Schwarz-Christoffel conformal mapping. *Sensors Actuators, A Phys.* 2004;113(1):106–17.
16. Koc CK, Ordung PF. Schwarz-Christoffel transformation for the simulation of two-dimensional capacitance. *IEEE Trans Comput Des Integr Circuits Syst.* 1989;8(9):1025–7.
17. Lee KW. Electromechanical Modelling of Trapezoidal Microstructures. Imperial College London; 2002.
18. Linear Technology. LT3468 Photoflash Capacitor Charger Datasheet [Internet]. Available from: <http://cds.linear.com/docs/en/datasheet/346812fa.pdf>
19. Williams J. High Voltage , Low Noise , DC/DC Converters. 2008;(March):9. Available from: <http://cds.linear.com/docs/en/application-note/an118fa.pdf>
20. Erickson R. The Flyback Converter - Lecture notes ECEN4517 [Internet]. Available from: <http://ecee.colorado.edu/ecen4517/materials/flyback.pdf>
21. Spengen WM Van, Oosterkamp TH. A sensitive electronic capacitance measurement system to measure the comb drive motion of surface micromachined MEMS devices. *J Micromechanics Microengineering.* 2007;17(4):828–34.
22. Von Wantoch T, Mallas C, Hofmann U, Janes J, Wagner B, Benecke W. Analysis of capacitive sensing for 2D-MEMS scanner laser projection. 2014;8977:897707. Available from:
<http://proceedings.spiedigitallibrary.org/proceeding.aspx?doi=10.1117/12.2038606>
23. Yang WQ, Stott a. L, Beck MS. High frequency and high resolution capacitance measuring circuit for process tomography. *IEE Proc - Circuits, Devices Syst.* 1994;141(3):215.
24. Fernández D, Madrenas J, Domínguez M, Pons J, Ricart J. Pulse drive and capacitance measurement circuit for MEMS electrostatic actuators. *Analog Integr Circuits Signal Process.* 2008;57(3):225–32.
25. Cagdaser B, Jog A, Last M. Capacitive sense feedback control for MEMS beam steering mirrors. *Solid-State Sensor, ... [Internet].* 2004;348–51. Available from: <http://citeseerx.ist.psu.edu/viewdoc/download?doi=10.1.1.113.4246&rep=rep1&type=pdf>

26. Reverter F, Gasulla M, Pallàs-Areny R. A low-cost microcontroller interface for low-value capacitive sensors. Conf Rec - IEEE Instrum Meas Technol Conf. 2004;3(May):1771–5.
27. Texas Instruments. FDC1004 4-Channel Capacitance-to-Digital Converter for Capacitive Sensing Solutions. datasheet. Revised April 2015. [Internet]. Available from: <http://www.ti.com/lit/ds/symlink/fdc1004.pdf>
28. Analog Devices. 24-Bit Capacitance-to-Digital Converter with Temperature Sensor. datasheet. 2007 [Internet]. Nonlinearity. 2007. Available from: <http://www.analog.com/media/en/technical-documentation/data-sheets/AD7747.pdf>
29. acam messelectronic gmbh: PicoCap [Internet]. Available from: <http://www.acam.de/products/picocap/>
30. ACAM. PCAP02A. Single-chip Solution for Capacitance Measurement. Volume 1. datasheet. Revised May 2014 [Internet]. Available from: http://www.acam.de/fileadmin/Download/pdf/PICOCAP/English/DB_PCap02A_Vol1_en.pdf

Appendix

All files for the project is available for download from the GitHub repository at:

https://github.com/kamratia1/FYP_2015

All the files are organised in the 4 folders below:

MATLAB Files	PCB Design Files	PICOCAP Documents and Config	Microcontroller Files
--------------	------------------	------------------------------	-----------------------

A. MATLAB Simulation Setup

In order to set up the simulation, the SC toolbox is required and available from: <http://www.math.udel.edu/~driscoll/SC/>

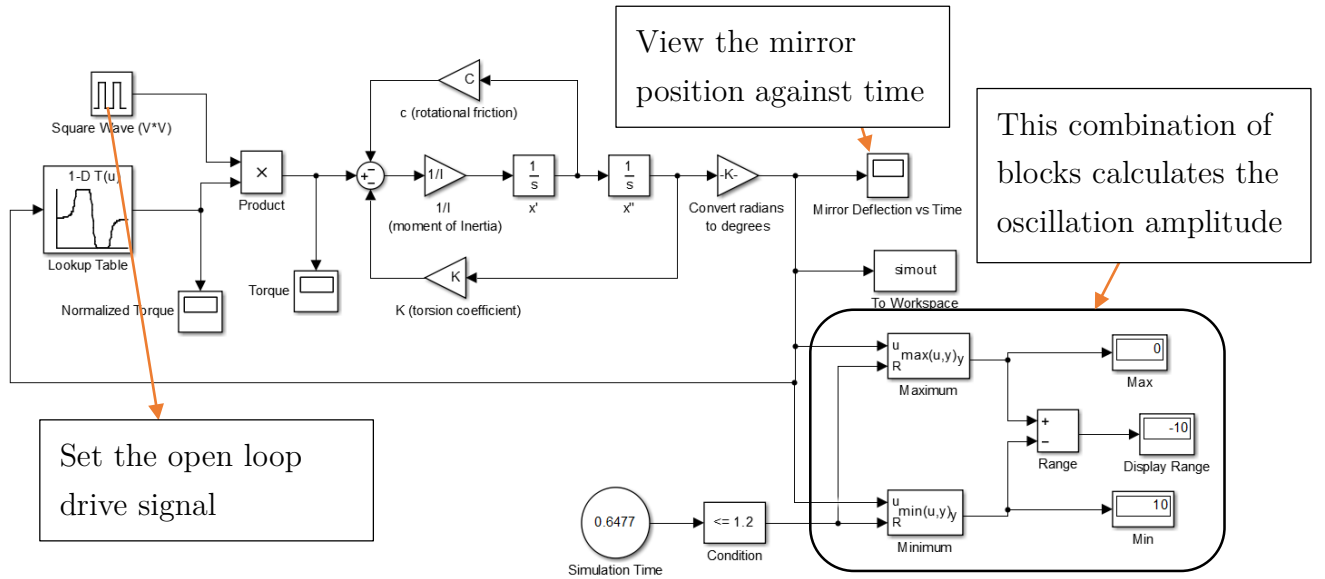
The MATLAB folder in the repository contains the following files:

- SCTransformation.m
- Rectmap.m
- calculate_constants.m
- FYP_Model_OpenLoop.slx
- FYP_Model_ClosedLoop.slx
- Simulink_Iterate.m
- Example_Data.mat

The files having the extensions .m represent MATLAB scripts that can be used to calculate data or plot graphs. The files with extensions .slx are simulink files. The file with a .mat extension is a MATLAB workspace file. The table below summarises all the MATLAB scripts and their purpose. Suitable comments are also available in the .m files for easy understanding.

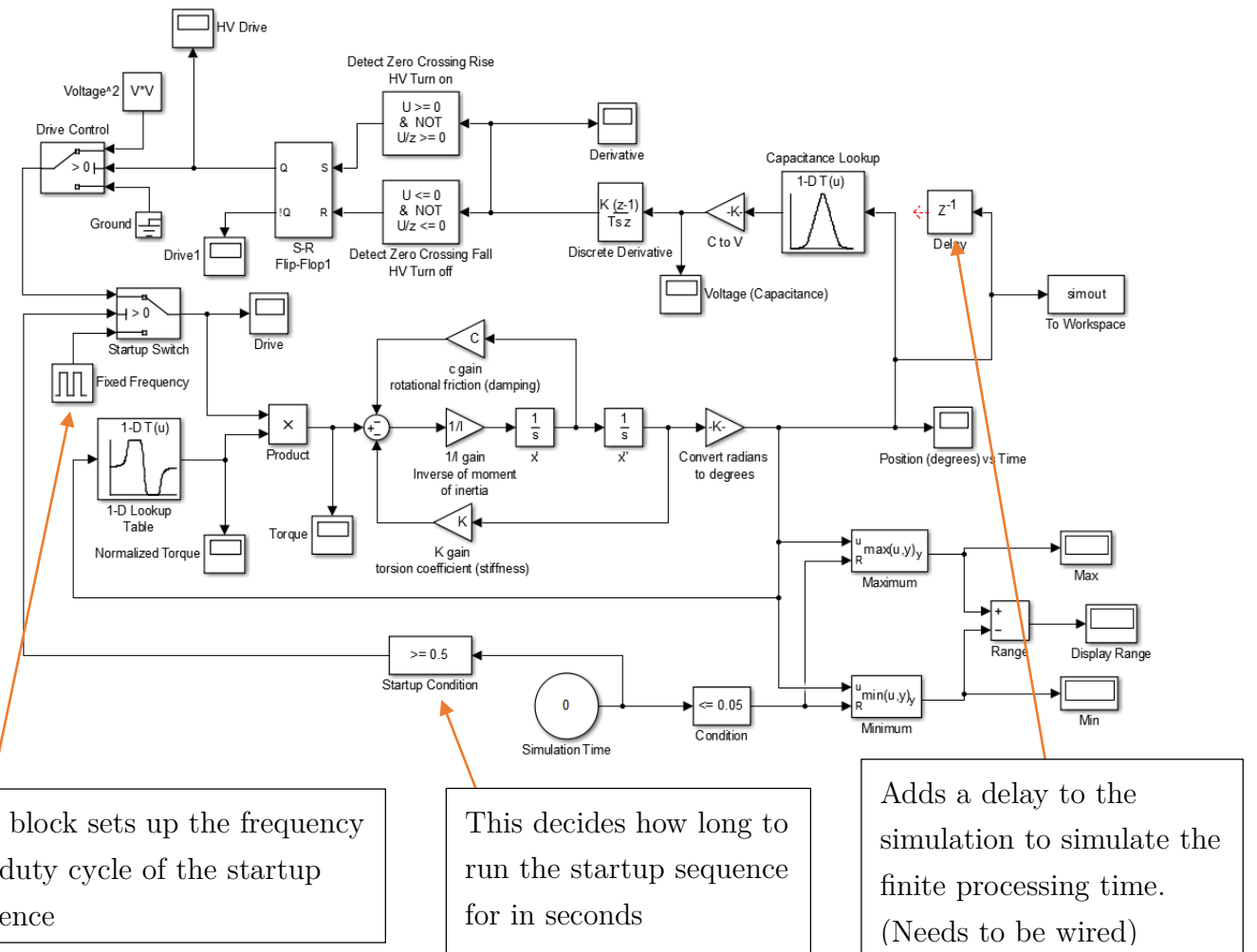
SCTransformation.m	Generates the torque function given the mirror dimensions.
Rectmap.m	Plots the SC Mapping between the z-plane and rectangular domain as shown in Figure 4.4. It requires the electrode geometry as input.
Calculate_constants.m	Calculates the constants I, C and K, given the mirror dimensions, Q and the resonant frequency.
Simulink_Iterate.m	Iterates through the closed loop Simulink simulation to produce a graph similar to Figure 4.13.
Example_Data.mat	Running this file will load data into the workspace in order to run the Simulink models. The data is for W=17mm, L=6mm, Q = 60

Open Loop Simulation (FYP_Model_OpenLoop.slx)



Closed Loop Simulation (FYP_Model_ClosedLoop.slx)

The sampling frequency of the system can be changed by adjusting the fixed step size in the configuration parameters of the model.

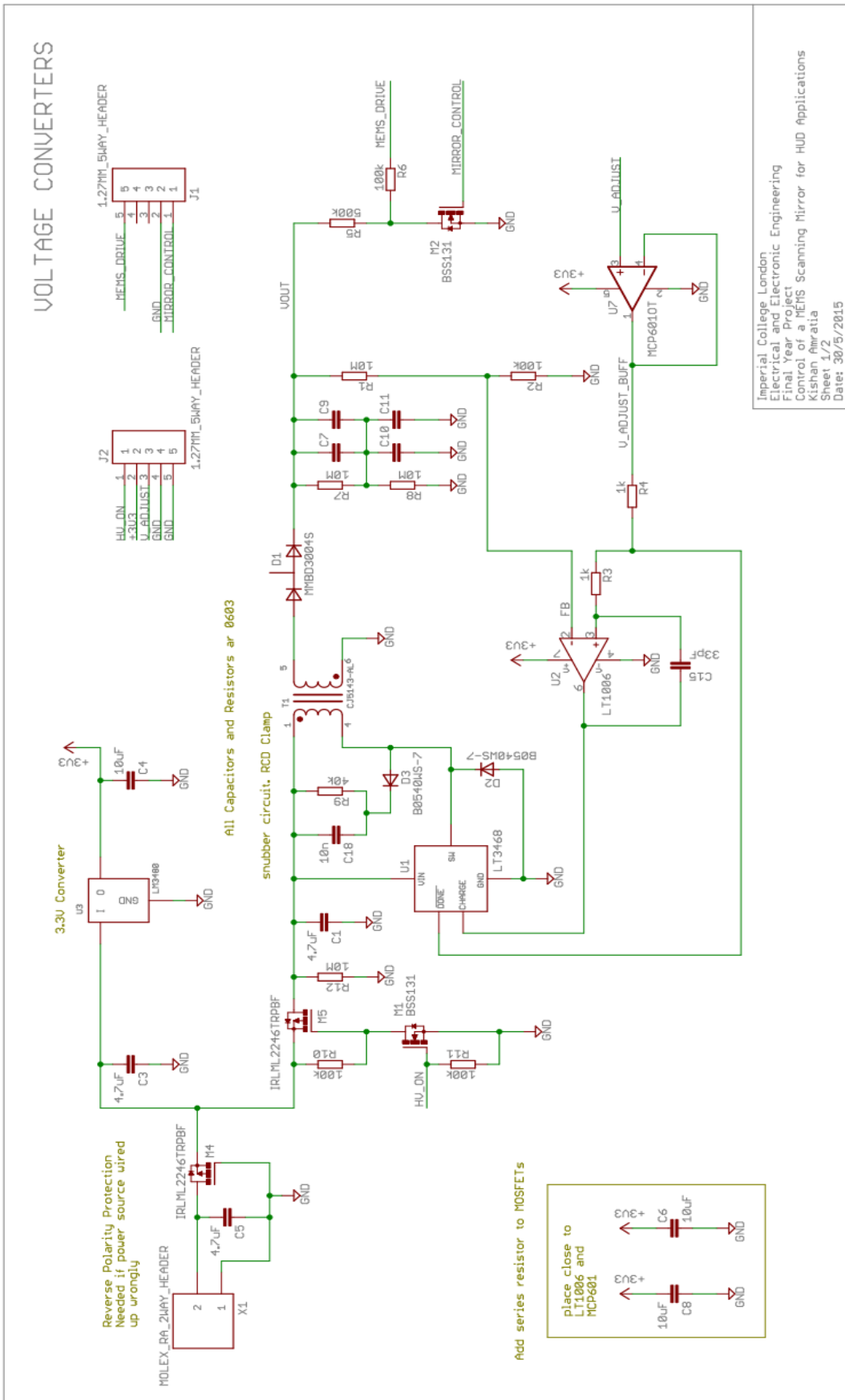


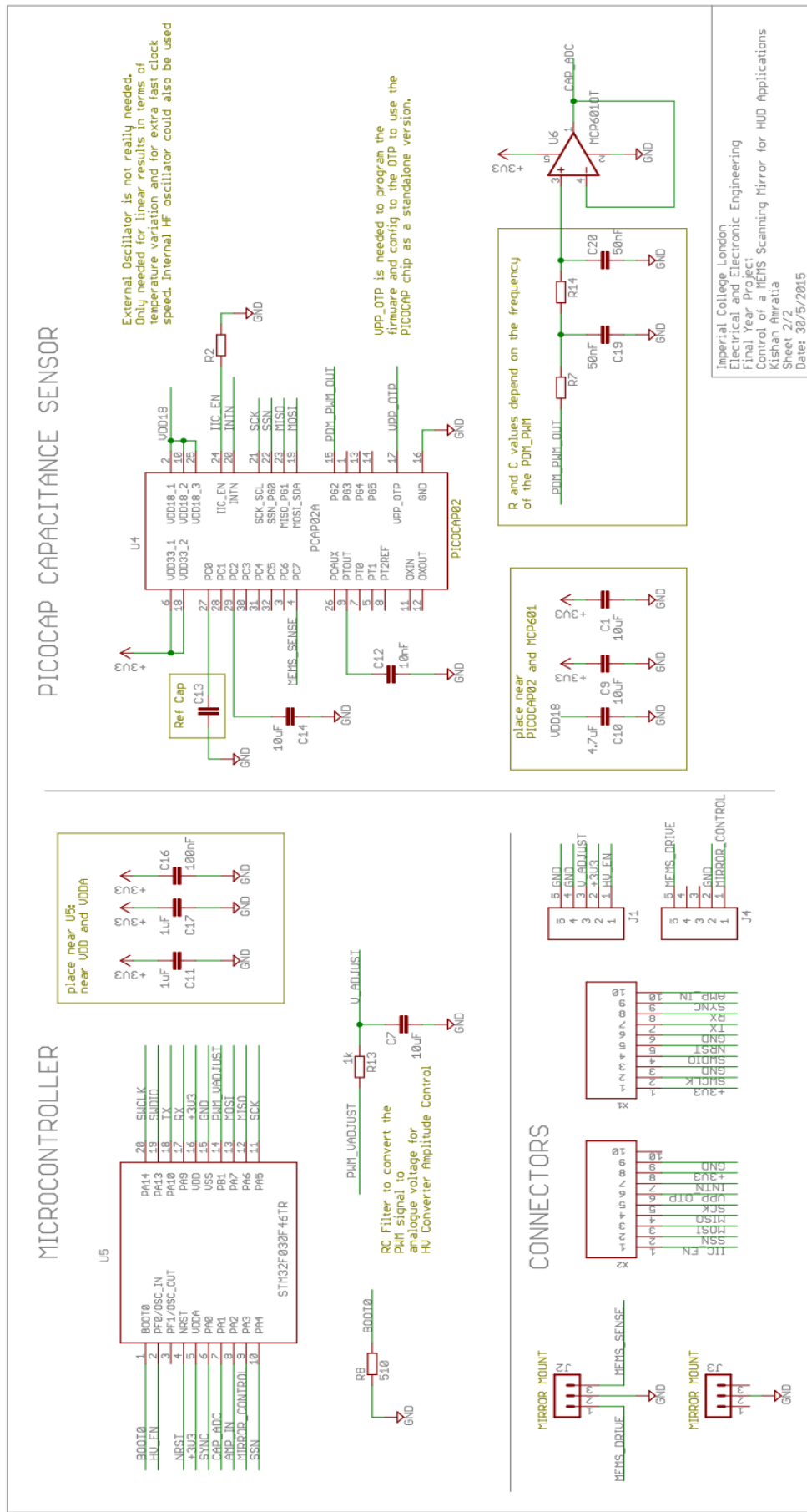
This block sets up the frequency and duty cycle of the startup sequence

This decides how long to run the startup sequence for in seconds

Adds a delay to the simulation to simulate the finite processing time.
(Needs to be wired)

B. Circuit Schematics





C. Notes on Circuit schematic and PCB design files

The “PCB Design Files” Folder in the repository contains three sub-folders:

- Initial Design: Contains the initial PCB design that is obsolete but provided anyway
- Final Design: Contains the design files for the final design of the board. There are two designs, one for the voltage converter board and the other for the digital board.
- Simulation: Contains the LTSpice simulation files for the HV Converter.

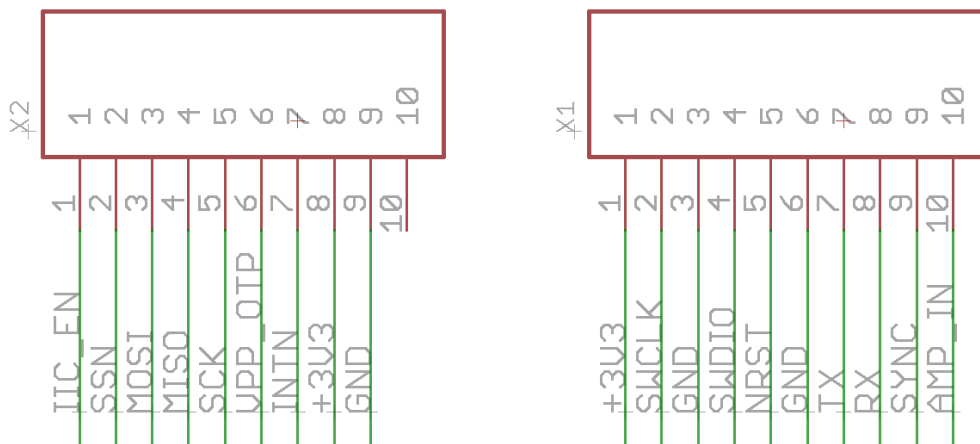
In order to open the PCB Design files, EAGLE Version 7.1 or above is required. This is freeware software available from: <http://www.cadsoftusa.com/index.php?id=5>

LTSpice is also freeware that can be downloaded from:

<http://www.linear.com/designtools/software/#LTspice>

Two 10-way FPC/FFC connectors are provided on the PCB to interface with the circuitry.

The schematic for this is shown below:



In order to communicate to the computer via the serial link, a USB FTDI TTL-232R cable should be used. It connects to X1 at pins 6, 7 and 8 corresponding to GND, TX and RX respectively.

Note: FTDI Drivers must be installed in order for the FTDI cable to be recognised by the computer and connected as a virtual COM port. The drivers can be downloaded from: <http://www.ftdichip.com/Drivers/VCP.htm>

D. Bill of Materials (BoM)

This BoM is not complete as it omits the passive components, however, all the ICs and connectors are included. The passive components i.e. the resistors and capacitors are all SMD packages in 0603 packages with at least 1% tolerance for the resistors unless otherwise stated in the schematic.

Voltage Converter PCB

Part	Part Number	Description	Manufacturer	Supplier	Order Code	Qty	Unit Price (£)
M1, M2	BSS131	N-Channel MOSFET, 100mA, 240V	Infineon	Farnell	1056524	2	0.06
M5, M4	IRLML2246 TRPBF	P-Channel MOSFET, 2.6A, 20V	International Rectifier	Farnell	1888166	2	0.0988
U1	LT3468ES5	Photoflash Cap Charger	Linear Technology	Farnell	1663829	1	3.86
U3	LM3480IM3 -3.3/NOPB	Linear Regulator 3.3V, 100mA	Texas Instruments	Farnell	1469102	1	1.2
T1	CJ5143- ALB	Flyback Transformer 1:15, 15uH	Coilcraft	Farnell	2458036	1	2.82
D3, D2	B0540WS-7	Schottky Rectifier 40V, 0.5A	Diodes Incorporated	Farnell	1773477	2	0.2
D1	MMBD3004 S-7-F	350V, 0.35W Series Diode Array (Min Order 25)	Diodes Incorporated	RS	751-4492	1	0.12
C7, C10, C9, C11	CGA9P3X7 S2A156M25 0KB	SMD 2220 Package Ceramic Capacitor 100V, 15uF	TDK	Farnell	2435508	4	1.3
U2	LT1006S8	Low Noise Operational Amplifier	Linear Technology	Farnell	9559230	1	3.12
U7	MCP601T- I/OT	General Purpose Single Op-Amp	MICROCHIP	Farnell	9758631	1	0.345
J1, J2	M52- 5000545	1.27mm Pitch Stacking Board Connectors Socket	HARWIN	Farnell	1099543	2	0.395
X1	353630260	2Way Right Angle Power Input Connector	MOLEX	Farnell	9289437	1	0.0894
	355070200	2Way Power Input Connector Socket	MOLEX	Farnell	7571550	1	0.0751
	502128100	Molex Crimp	MOLEX	Farnell	7571640	2	0.101

Digital Board PCB

Part	Part Number	Description	Manufacturer	Supplier	Order Code	Qty	Unit Price (£)
U5	STM32F030F4P6TR	ARM Cortex M0 Microcontroller	ST Microelectronics	Farnell	2432084	1	0.878
J2, J3	22-28-4036	3 way 2.54mm pitch Header	MOLEX	Farnell	1444318	2	0.06
J1, J4	M52-040023V0545	1.27mm Pitch Stacking Board Connectors Header	HARWIN	Farnell	1099560	2	0.406
X1, X2	XF2M10151A	10Way FPC Connector 0.5mm Pitch	OMRON	Farnell	1112555	2	0.563
U4	PCAP02AE	PICOCAP2 Digital Capacitance Sensor Chip	ACAM Messelectronic gmbh	Solid State Supplies 2001	PCAP02AE	1	8.64
U6	MCP601TI/OT	General Purpose Single Op-Amp	MICROCHIP	Farnell	9758631	1	0.345

E. Microcontroller Software Setup and Programming

The “Microcontroller Files” folder in the repository contains 3 subfolders:

- ATTEL ATTiny (old uC): Contains files for old microcontroller
- STM32: Contains files for new microcontroller
- PythonGUI: Contains the GUI application that communicates to the hardware via the serial port

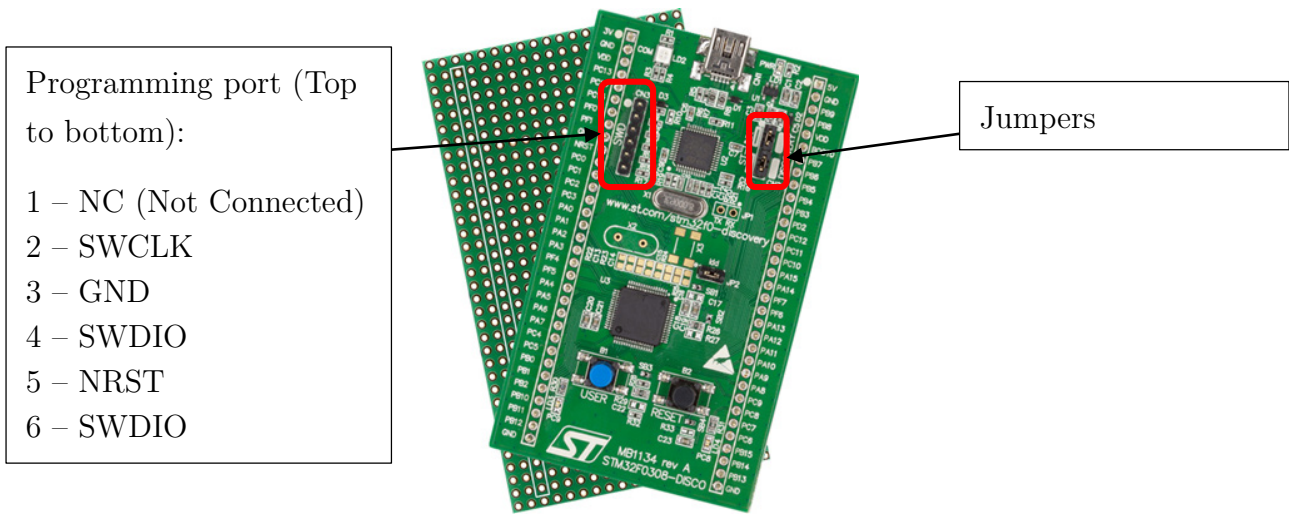
In order to program the old microcontroller, ATTEL Studio 6.2 or higher is required. It is available from: <http://www.atmel.com/tools/atmelstudio.aspx>

The software for the microcontroller was developed on the STM32F0308-Discovery board. The IDE used was the free version of Keil uVision 5 which can be downloaded from: <https://www.keil.com/demo/eval/arm.htm>

Note: Keil uVision5 requires registration in order to download it.

Programming the microcontroller on the final PCB

Below is an image of the development board showing the programming port (SWD – Software Debug) and the Jumpers



In order to program an external device such as on the PCB, the jumpers need to be disconnected and the programming port needs to be connected to X1 shown in Appendix C to the corresponding pins on the Programming port. The schematic for the development board and more information about it can be found at:

<http://www.st.com/web/en/catalog/tools/PF259100>

When programming the chip on the development board, the jumpers need to be placed back.

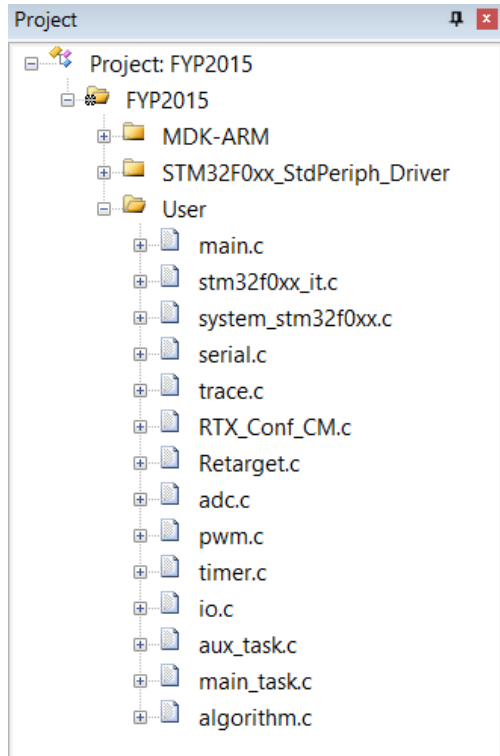
The uVision project file for the microcontroller software is written for the microcontroller on the development board (STM32F030R8). Since the microcontroller on the PCB is slightly different, the target options for the project need to be changed when programming the new chip. This can be done by following the following steps:

- Select Project -> Options for Target
- In the Device Menu, select STM32F030F4. Changing the device, changes some of the other settings and in the other options that are necessary to program the device.
- In the Target Menu, Ensure the Operating System is selected as RTX Kernel
- In the Debug Menu, ensure that ST-Link Debugger is selected and the Use radio button selected as well.

In case the settings get changed. Some screenshots of all the target options are available in the document “Target_options.pdf” in the “STM32” folder.

STM32 Microcontroller Code

The microcontroller code is written in the C language. The folder structure in the IDE is organised such that all written code is in the folder “User” as shown below. All the libraries required are in the other folders (MDK-ARM and STM32F0xx_StdPeriph_Driver).



All code is commented as much as possible to help in understanding it.

Below is a table giving a short description of each of the files:

main.c	This file contains the main function that sets up the threads for the RTOS.
stm32f0xx_it.c	Contains the interrupt vectors
serial.c	Contains low level code for UART communication
trace.c	Contains trace debugging functions for printing to serial
adc.c	Contains setup code for the adc
pwm.c	Contains setup code for the PWM for the HV converter control
timer.c	Contains setup function for the interrupt timers and other timers
io.c	Contains setup code for input/output pins
aux_task.c	Contains the code for the auxiliary thread which runs the debugging and serial interface to the PC.
main_task.c	Contains the code for the main thread which runs the control algorithm
algorithm.c	Contains the code for the control algorithm
Config.h	This file contains all pin definitions and definitions of constants

Note that most of the files will also have relevant header files that contain function prototypes and some constants that are defined.

Python GUI

The python GUI application requires python 2.7 which can be downloaded from: <https://www.python.org/download/releases/2.7/>

It also requires pyQt which is the framework that runs the GUI. pyQt for windows can be downloaded from <http://sourceforge.net/projects/pyqt/files/PyQt4/>

Also, to allow serial communication via a virtual COM port on windows, the pySerial library needs to be installed. This can be downloaded from:

<http://sourceforge.net/projects/pyserial/files/pyserial/2.7/>

To run the program, the python file “demo.py” inside the “Python GUI” subfolder needs to be executed. Note that in order for it to work, a virtual COM port must be available to connect to.

F. PICOCAP Device Programming and using the GUI

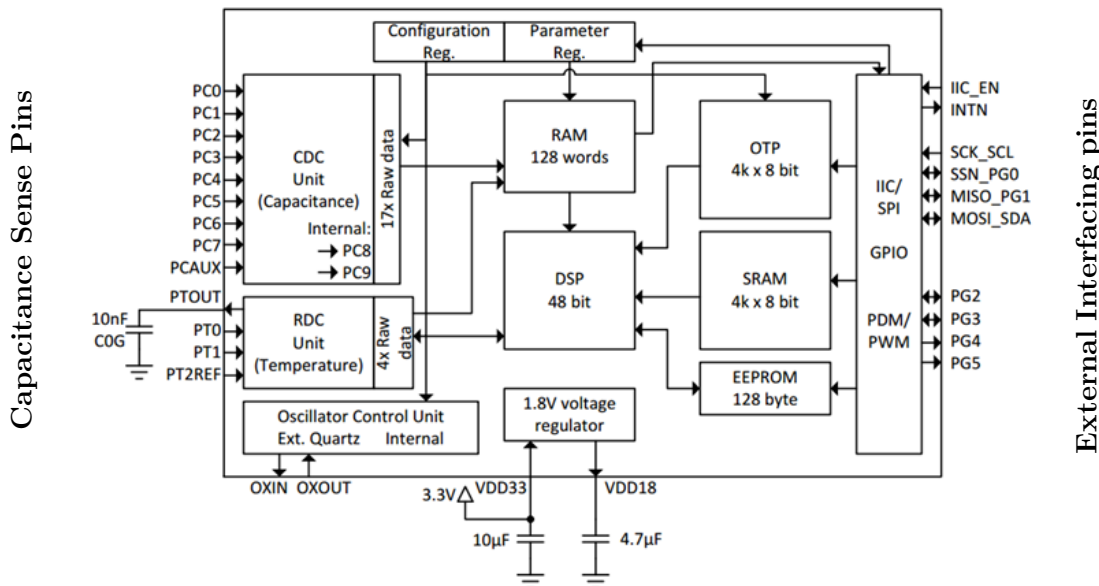
All files and documents for using the capacitance sensor is in the folder “PICOCAP documents and config” in the repository.

This is split further into 3 sub-folders:

- Windows Software: Contains the installation files for the windows software to interface with the device. *Note: it only works with Windows 7*
- Docs: Contains the datasheets and all documentation of the chip
- Config: Contains configuration files to set the registers in the device for measuring capacitance data from the mirror.

Properties and Basic features of the PICOCAP

The PICOCAP capacitance sensor chip is a complex device which offers a lot of flexibility. The datasheet of the device is very long and can be difficult to obtain the right information. This section is therefore written to help in understanding the basic features of the chip that is used in this project. The figure below (from the datasheet) is a block diagram of the chip showing the internal peripherals.



In this project, the capacitance sensor is used in single-grounded mode whereby the capacitance to be sensed is connected between one of the capacitance sense pins (PC0 to PC7) and ground. It is also capable to measure differential capacitance.

For basic operation, it must have some firmware loaded in the Static-Random-Access-Memory (SRAM) along with the configuration registers set as required by the user. Standard firmware and configuration is available from the manufacturer and can be used to

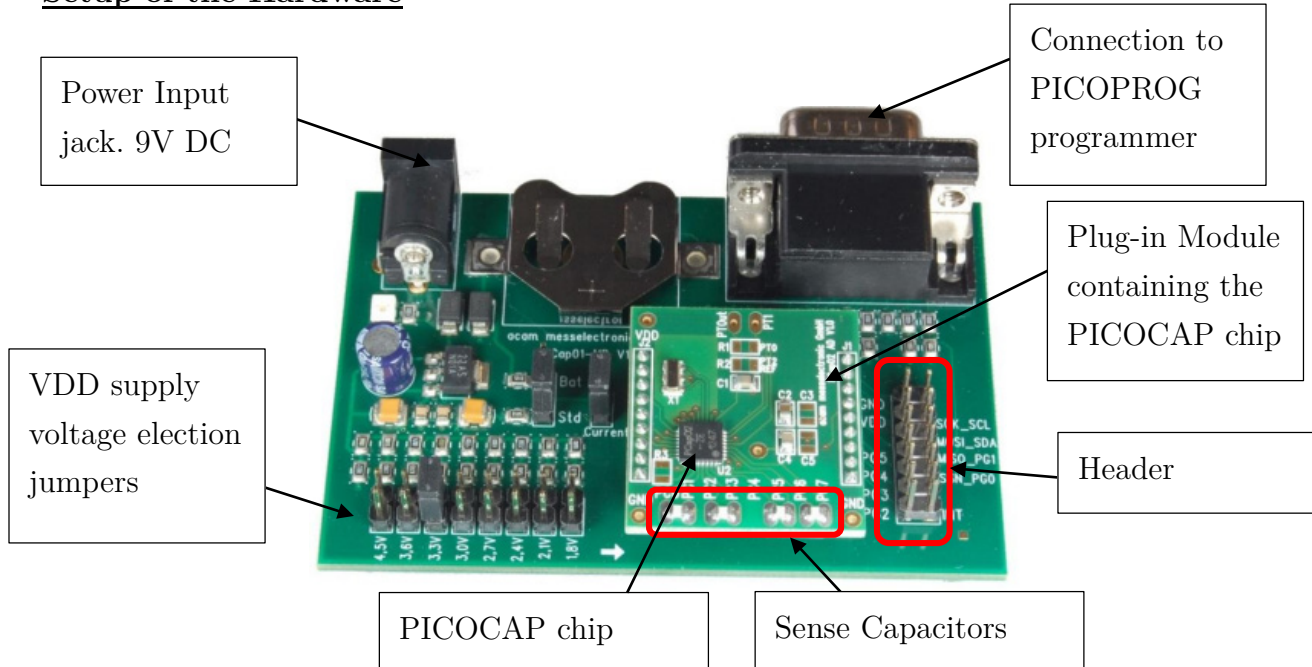
perform simple capacitance measurements. The table below describes the different features of the chip.

Feature	Description
CDC	This is the Capacitance to Digital Converter (CDC) unit which measures capacitance of any device connected at pins PC0-PC7. It does this by measuring the discharge time through a fixed internal resistor of the sense capacitor and a reference capacitor.
RDC	This is a Resistance to Digital converter (RDC) which is used for measuring temperature accurately.
DSP	The PICOCAP has a 48-Bit Digital Signal Processor which does all the digital processing in the chip. It is used for filtering, averaging and sensor linearization. There is a specific instruction set that can be used by the user if needed. However, the standard firmware provided by the manufacturer is enough to perform capacitance readings and therefore detailed understanding of the instruction set is not necessary.
Configuration and Parameter Registers	There are 51 configuration registers used for configuring the hardware. This includes the parameters for the CDC, the clocks, Pulse-Coded-Generation and some control over the interfacing with the DSP. There are 27 registers to make parameters available for the DSP. All of these registers are 8 bits long. (See Chapter 5 of the datasheet)
RAM	Random Access Memory. The DSP uses this memory to load and store data while processing the instructions. There are also 44 bytes in the RAM kept for storing the results of the conversions from the CDC and RDC.
SRAM	This is where the firmware is stored which interacts with the DSP to perform the conversions
OTP	This is a block of flash memory of size 32kB that is only one-time-programmable (OTP). Its purpose is to permanently store the firmware and configuration data that can be loaded into the SRAM and configuration registers respectively during power-on of the device. It is used mainly when the PICOCAP is to be used as a standalone device.
EEPROM	This is a 128 byte Electrically Erasable Programmable Read-Only Memory. This can be used for storing calibration data for the sensors.
External Interfacing	External interfacing to a microcontroller to read data from the chip can be done through SPI or I ² C. It can also be programmed through any of these protocols. There are also GPIO pins available for using interrupts or switching of external devices. These pins can also be used to generate a pulse-coded-generation output which outputs the value of the capacitance using PWM or PDM.

There are two methods to interface with the chip using SPI or I²C through a microcontroller. In this project, SPI should be used since it allows a faster mode of communication between the chip and the microcontroller to ensure that the capacitance measuring rate is not limited by the communication speed which could be the case if using I²C.

The chip also has two Pulse-coded-generation outputs: PWM and PDM that correspond to the reading of any capacitance input pin (PC0 to PC7). These outputs can be low-pass filtered to acquire a pure analogue signal that corresponds to the sense capacitance.

Setup of the Hardware



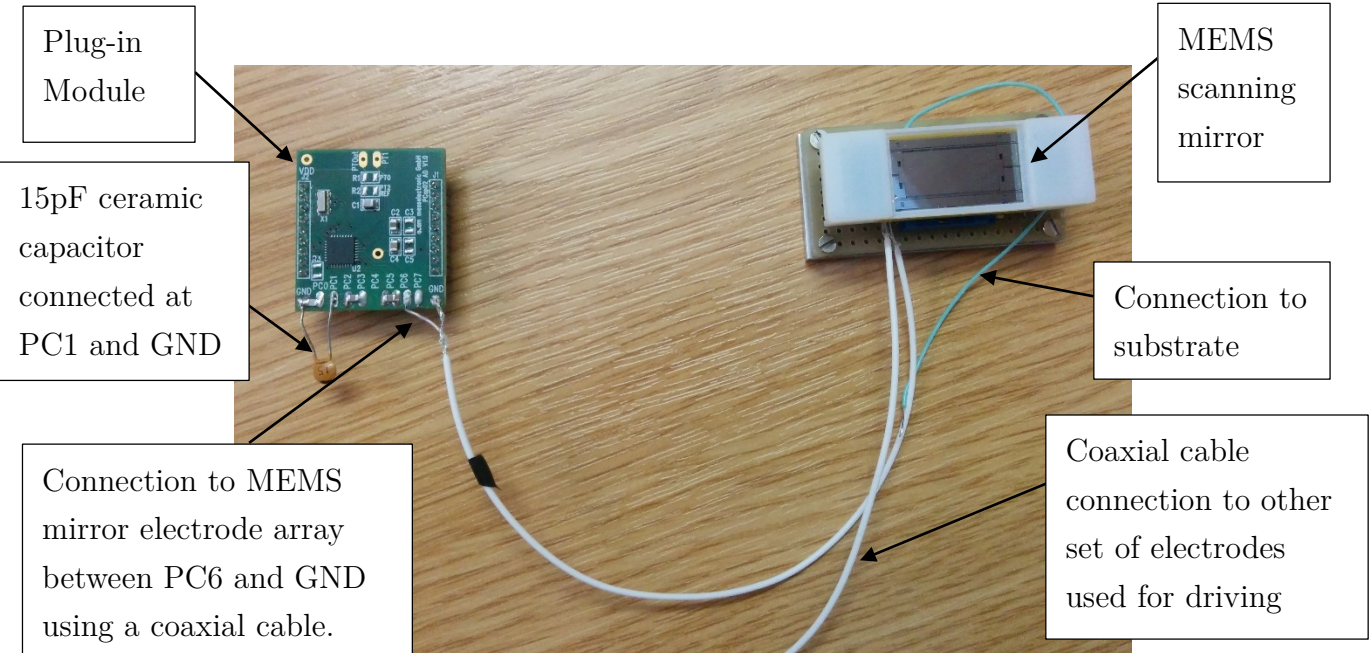
The figure above shows an image of the development board. The Plug-in module contains the PICOCAP chip, which can be taken and easily plugged back in. The PICOPROG programmer for the development board is shown below. It needs to be connected between a PC and the development board.



GND	VPP OTP
VDD	SCK SCL
	MOSI SDA
PG5	MISO PG1
PG4	SSN PGO
PG3	IIC EN
PG2	INT

The pin header on the development board has been modified slightly to access some of the pins from the Plug-in module. The pinout of the header is shown in the table above.

When performing tests for the project. The MEMS mirror was connected to between PC6 and ground on the plug in module as shown below.



Using the PICOCAP Evaluation Software

The PICOCAP evaluation software was used to program the device and set the parameters for measurement. In this project, the parameters used are saved in the file “FYP_config.cfg” in the “Config” folder in the repository.

These YouTube videos from the manufacturer can help with the start-up and how to use the development environment and the evaluation software:

https://www.youtube.com/watch?v=TR7I-c_vwok

<https://www.youtube.com/watch?v=fe2S-QSWRMo>

Note: When the PDM/PWM interface is setup and at the same time, if the “Start Measurement” button is pressed in the software, the capacitance readings can have some non-uniform periodic spikes. Therefore, to ensure that the capacitance signal is not too noisy with the spikes, only use one of the measuring methods either PDM/PWM or the SPI interface via the evaluation software.

Programming the PICOCAP on the PCB

There are two methods to program the PICOCAP chip. One is to use the SPI interface from the microcontroller to program the device. This requires implementation of the code to do this, which is described in the PICOCAP Datasheet.

The other method is to use the development kit environment. The header provided on the development board will need to connect to the corresponding pins on connector X2 shown in Appendix B. Note that the PICOCAP plug-in module needs to be removed in order to do this.

In terms of programming, if the firmware and configuration is written to the OTP flash, the chip can be used standalone without the need to program it again. Note that the OTP is one-time programmable and additional changes to the flash cannot be made.

In the plug-in module used in this project, the OTP flash has been programmed with the standard firmware. This means that the firmware for the device cannot be changed, unless it is programmed into the SRAM every time it is powered-on. The Config has not been programmed into the OTP flash, therefore this needs to be programmed every time the device is turned on.